Clim Dyn (2012) 39:2631–2657
DOI 10.1007/s00382-011-1239-2

# A look at the ocean in the EC-Earth climate model

**Andreas Sterl · Richard Bintanja · Laurent Brodeau · Emily Gleeson · Torben Koenigk · Torben Schmith · Tido Semmler · Camiel Severijns · Klaus Wyser · Shuting Yang**

Received: 29 June 2011 / Accepted: 30 October 2011 / Published online: 13 November 2011
© Springer-Verlag 2011

**Abstract** EC-Earth is a newly developed global climate system model. Its core components are the Integrated Forecast System (IFS) of the European Centre for Medium Range Weather Forecasts (ECMWF) as the atmosphere component and the Nucleus for European Modelling of the Ocean (NEMO) developed by Institute Pierre Simon Laplace (IPSL) as the ocean component. Both components are used with a horizontal resolution of roughly one degree. In this paper we describe the performance of NEMO in the coupled system by comparing model output with ocean observations. We concentrate on the surface ocean and mass transports. It appears that in general the model has a cold and fresh bias, but a much too warm Southern Ocean. While sea ice concentration and extent have realistic values, the ice tends to be too thick along the Siberian coast. Transports through important straits have realistic values, but generally are at the lower end of the range of observational estimates. Exceptions are very narrow straits (Gibraltar, Bering) which are too wide due to the limited resolution. Consequently the modelled transports through them are too high. The strength of the Atlantic meridional overturning circulation is also at the lower end of observational estimates. The interannual variability of key variables and correlations between them are realistic in size and pattern. This is especially true for the variability of surface temperature in the tropical Pacific (El Niño). Overall the ocean component of EC-Earth performs well and helps making EC-Earth a reliable climate model.

**Keywords** Climate model · NEMO ocean model: general ocean circulation · Surface fluxes · Sea ice · Ocean heat transport

This paper is a contribution to the special issue on EC-Earth, a global climate and earth system model based on the seasonal forecast system of the European Centre for Medium-Range Weather Forecasts, and developed by the international EC-Earth consortium. This special issue is coordinated by Wilco Hazeleger (chair of the EC-Earth consortium) and Richard Bintanja.

A. Sterl (✉) · R. Bintanja · C. Severijns
Royal Netherlands Meteorological Institute (KNMI),
P.O. Box 201, 3730 AE De Bilt, Netherlands
e-mail: sterl@knmi.nl

L. Brodeau
Department of Meteorology,
Stockholm University, Stockholm, Sweden

E. Gleeson · T. Semmler
Met Éireann, Dublin, Ireland

T. Koenigk · K. Wyser
Swedish Meteorological and Hydrological Institute (SMHI),
Norrköping, Sweden

T. Schmith · S. Yang
Danish Meteorological Institute (DMI), Copenhagen, Denmark

## 1 Introduction

Societies are dependent on, and adapted to, their local climate for a wide range of activities, from farming practices and water availability to health and living conditions. This also means that societies are vulnerable to climate changes, be it caused by natural variability or anthropogenic activity. Information about future (changes of) climate is therefore important to take timely adaptation measures.

Climate arises from a complex interplay between atmosphere, ocean, ice and soil. Besides physical processes (e.g., radiation, energy transport) also chemical (e.g., ozone destruction) and biological (e.g., $CO_2$ uptake by plants or

phytoplankton) processes are involved. To study such complex interactions, Earth System Models (ESM) are used. In an ESM all these processes and their interactions are modelled numerically, that is, by a computer code which is based on a mathematical description of the relevant processes.

Traditionally, a distinction between weather (short-term variability of the atmosphere) and climate (long-term statistics of weather) is made, and modelling them has been performed by different scientific communities. However, many processes behind both are the same, and the use of one "seamless prediction" model for weather and climate on scales from days to centuries would serve both communities (Hazeleger et al. 2010). To achieve this, a consortium of Earth-system scientists from 10 European countries have started to develop EC-Earth, an ESM based on the seasonal forecasting model of the European Centre for Medium Range Weather Forecasts (ECMWF). Based on a state-of-the-art weather forecast model, this modelling system is envisaged to open the way to a "seamless predicting" ESM.

Currently EC-Earth consists of models describing the physical processes in atmosphere, ocean, sea ice and the land surface, while chemical and biological components are under development (Hazeleger et al. 2010). In this paper we describe the performance of the ocean component of EC-Earth and its interaction with the atmosphere in a long (centuries) run under present-day forcing conditions. Where appropriate we also show results from a run performed under pre-industrial forcing conditions.

## 2 Model description

### 2.1 The coupled EC-Earth system

The core of EC-Earth is formed by the Integrated Forecast System (IFS) of the European Centre for Medium Range Weather Forecasts (ECMWF) as the atmosphere component (ECMWF 2006) and the Nucleus for European Modelling of the Ocean (NEMO) developed by Institute Pierre Simon Laplace (IPSL) as the ocean component (Madec 2008). Integrated into NEMO is the Louvain-la-Neuve Sea Ice Model (LIM) that has been developed at the University of Louvain-la-Neuve (Fichefet and Morales Maqueda 1997; Bouillon et al. 2009). The atmosphere and ocean/sea ice parts are coupled through the OASIS3 (Ocean, Atmosphere, Sea Ice, Soil version 3) coupler developed at the Centre Européen de Recherche et Formation Avancées en Calcul Scientifique (CERFACS) (Valcke 2006). This core will be extended to become an Earth System Model (ESM) by adding models for other geophysical system components like the carbon cycle, vegetation and atmospheric chemistry (Hazeleger et al. 2010).

The experiments assessed in this paper have been performed with EC-Earth v2.2. It is a close predecessor of v2.3, which is used to perform CMIP5 runs. The following subsections give a short description of the component models. The reader not interested in technical details may wish to jump directly to Sect. 3.

### 2.2 IFS, the atmosphere component of EC-Earth

IFS is the atmosphere model used operationally at ECMWF to perform medium-range (10 days) to seasonal forecasts. It is a spectral model with triangular truncation. The model is available with a variety of different truncations. Compared with the T1279 truncation, corresponding to about 16 km, that is used for the operational medium-range (10 days) forecasts, EC-Earth uses a relatively coarse truncation of T159, which is roughly equivalent to 125 km. In the vertical 62 levels of a terrain-following mixed $\sigma$/pressure coordinate are used. The lowest model level is at a height of 30 m above the ground, and the highest level is at 5 hPa. The use of a semi-Lagrangian advection scheme makes it possible to use a time step of 1 h in the T159 version of EC-Earth.

The current version of EC-Earth (v2.2) is based on cycle 31r1 of IFS (ECMWF 2006), but some improvements from later cycles have been added. The most important ones are a new convection scheme (Bechtold et al. 2008), the new land surface scheme H-TESSEL (Balsamo et al. 2009), and a new snow scheme (Dutra et al. 2010). The latter reformulates the density of snow and the representation of liquid water in the snow pack, reducing warm biases (Hazeleger et al. 2010, their Figure 5). A description of results from the atmospheric part of EC-Earth (i.e., IFS) can be found in the paper of Hazeleger et al. (2011) in this issue.

### 2.3 NEMO, the ocean component of EC-Earth

The ocean component of EC-Earth is version 2.2 of NEMO (Madec 2008), a primitive equation ocean general circulation model with a free surface. That the several years old version 2.2 is used results from the fact that EC-Earth evolved from earlier work done by ECMWF's seasonal forecasting group (Hazeleger et al. 2010). Work on a new EC-Earth version (v3) including an up-to-date NEMO version is under way (see Sect. 6).

In NEMO the horizontal discretization is done on a curvilinear C-grid (Arakawa and Lamb 1977), while in the vertical a z-coordinate is used. The model allows for various choices for the physical parametrization as well as the numerical algorithms. The most important choices made for EC-Earth are for the Turbulent Kinetic Energy (TKE) scheme for vertical mixing, a partial step implementation for the z-coordinate (grid boxes do not continue below

topography), a bottom boundary scheme to mix dense water down a slope (e.g., Denmark Strait overflow water or Mediteranean outflow), and the use of the Total Variance Dissipation (TVD) or Flux Corrected Transport (FCT) scheme for horizontal advection, which is positive definite and thus cannot produce spurious negative values. Horizontal tracer diffusion is described by the Gent-McWilliams (Gent and McWilliams 1990) parametrization of eddy-induced turbulence. Details of these parametrization are described in Madec (2008). Values for some key parameters used in EC-Earth are listed in Table 1, and a complete list can be found at http://ecearth.knmi.nl/index.php?n=PmWiki.Pre-IndustrialControlRun under "namelists".

The configuration of NEMO is very flexible, allowing for mesh refinements in areas of interest. For EC-Earth the ORCA1 configuration (see http://www.noc.soton.ac.uk/nemo) is used. It has a basic resolution of 1° × 1° with a meridional refinement to 1/3° at the equator. The singularity at the North Pole is avoided by use of a tripolar grid with poles over land (Siberia, Canada, Antarctica). The thickness of the 42 layers increases from 10 m in the upper 100–300 m at depth. The deepest layer has its centre at 5,350 m and reaches down to 5,500 m.

Figure 1 shows the model bathymetry. Regions where the real ocean is deeper than the maximum model depth of 5500 m are marked red. The bathymetry was derived from the ETOPO2 data set (see http://www.ngdc.noaa.gov/mgg/fliers/01mgg04.html) with additions from other sources near Antarctica. Some manual adjustments had to be made to ensure the presence of narrow sills. For details see the ORCA1 web site at http://www.noc.soton.ac.uk/nemo. In Fig. 1a the bathymetry is plotted on the ORCA1 model grid together with the geographical latitudes and longitudes. The two poles and the grid refinement near the equator are clearly visible. Figure 1b shows the same field in geographical latitude/longitude coordinates.

### 2.4 LIM, the sea-ice component of EC-Earth

The LIM sea ice model (Fichefet and Morales Maqueda 1997; Bouillon et al. 2009) is part of the NEMO distribution. It uses the same grid as the ocean model. Of the two versions that are available the one-layer LIM2 version is used in the current version of EC-Earth. Mechanically, it models sea ice as a two-dimensional (i.e., one layer) viscous-plastic continuum that transmits stresses between the ocean and the atmosphere. Thermodynamically, it consists of two layers, an ice layer with a snow layer on top of it. Subgrid-scale parametrizations account for heat storage, heat conduction, snow-ice transformation, non-uniform snow and ice distributions, and albedo. The full model description can be found in Fichefet and Morales Maqueda (1997), and a complete list of parameter values used in EC-Earth can be found at http://ecearth.knmi.nl/index.php?n=PmWiki.Pre-IndustrialControlRun under "namelist_ice".

**Table 1** Values of some key parameters as used in EC-Earth

| Parameter | Value | Unit |
|---|---|---|
| Time step | 3,600 | s |
| Horizontal eddy diffusivity | $10^3$ | $m^2/s$ |
| Horizontal eddy induced velocity coefficient | $10^3$ | $m^2/s$ |
| Horizontal eddy viscosity | $10^4$ | $m^2/s$ |
| Vertical eddy diffusivity | $10^{-5}$ | $m^2/s$ |
| Vertical eddy viscosity | $10^{-4}$ | $m^2/s$ |
| Coef. of the surface input of TKE (ebb) (TKE input = ebb $\lvert\tau\rvert/\rho$) | 60 | – |

### 2.5 The coupling strategy

The coupling software OASIS3 (Valcke 2006) is used to couple IFS to NEMO/LIM. OASIS3 synchronizes the two models and interpolates fields between the respective grids. Both IFS and NEMO employ a time step of 1 h, while a time step of 3 h is used for LIM. Therefore, coupling is also done every 3 h, and exchanged fields are held constant for the time steps between coupling. From NEMO/LIM sea ice concentration, thickness of snow on sea ice, ice albedo and surface temperature (sea, ice) are passed to IFS, while fluxes of heat, freshwater and momentum are passed the other way.

In IFS eight different surface types (tiles) are distinguished within one grid box, and accordingly eight different fluxes are calculated. To conserve fluxes during interpolation from the atmosphere to the ocean grid, not the fluxes, but the tile-fraction weighted fluxes, together with the tile fractions themselves, are passed to the ocean and recombined to give fluxes on the ocean grid. Details of this procedure are given in Appendix A.

## 3 Evaluation of the mean ocean state and its variability

### 3.1 Runs

In this section we present long-term means of some key oceanic variables as simulated by EC-Earth and compare them with available observations to assess the performance of the model. The results are from a run performed under present-day (PD) forcing, meaning greenhouse-gas (GHG) and aerosol concentrations representative for the year 2000. Where appropriate, we also show differences of the PD run with results from a run performed under pre-industrial (PI) conditions, i.e., GHG and aerosol concentrations representative for 1850.

The ocean initial conditions for both the PD and the PI runs were taken from a coupled spin-up run performed

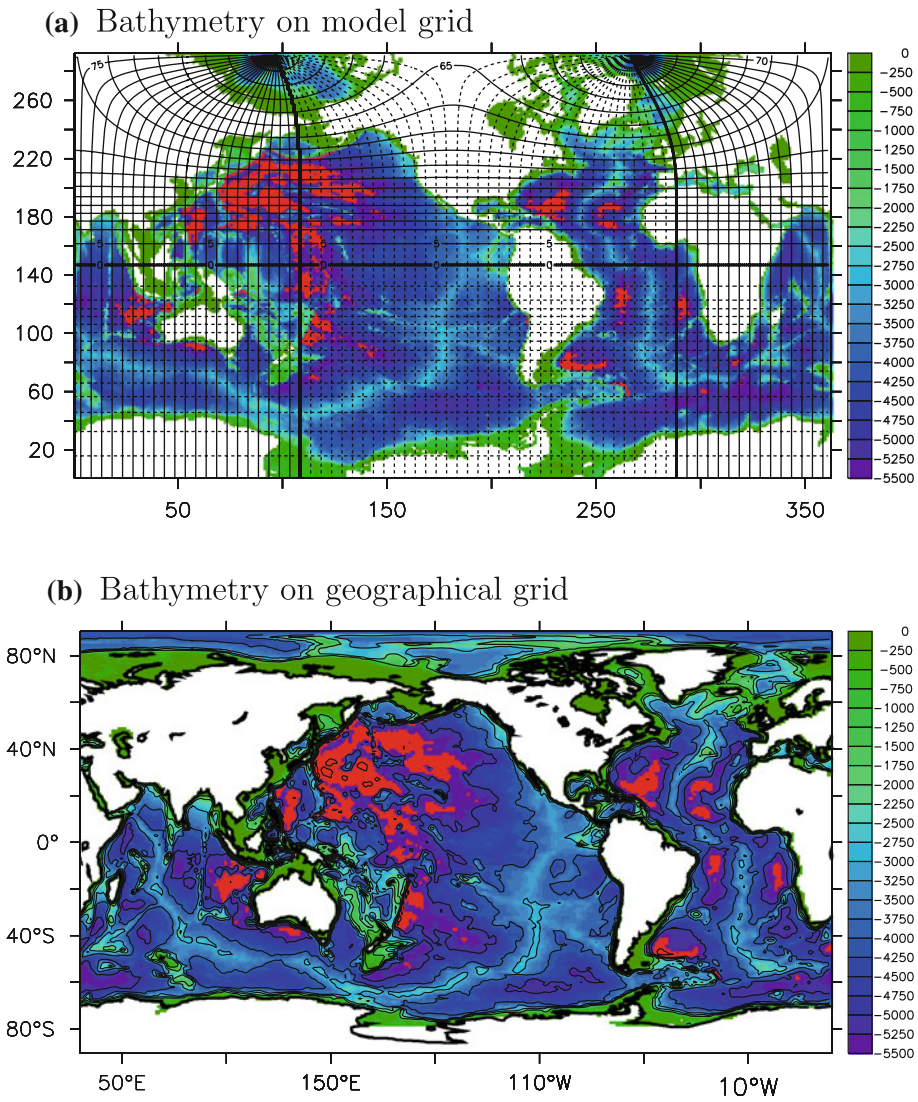


**Fig. 1** Model ocean depth (in m) on **a** the model grid (T points) and **b** in geographical coordinates. In the *red* areas the actual ocean depth is deeper than the maximum model depth of 5,500 m. In **a** the geographical latitude/longitude grid is overlayed in *black*, and in **b** *black contours* are added every km for reference

under present-day conditions. During the first part of the spin-up run the model version was not yet frozen and some improvements in the coupling were introduced. For the PD run the atmosphere was initialized with data from ERA-interim of 1st January, 2000. The PD run was run for 440 years, and the PI run for 600 years. Unless otherwise stated, we here use data from the last 100 years of the runs.

In Sect. 4 we additionally show one result from another run performed under PI forcing, but starting from different initial conditions. We do so because this run exhibits an interesting cold event in the North Atlantic area that lasts for about 100 years. This cold event will be fully described in a paper by Gleeson et al. (in preparation).

### 3.2 Ocean temperature and salinity

The runs are too short to have reached stationarity. Figure 2 shows the linear trends of temperature and salinity as calculated over the last 264 years of the PD run for two different depth ranges as well as for the section along 30°W in the Atlantic Ocean. The upper 500 m show a general warming with some isolated areas of cooling (Fig. 2a) and a strong freshening (Fig. 2b). The deeper layers (Fig. 2c, d) exhibit a general warming and salinification, which is largest around Antarctica. In the Atlantic Ocean the trends are different. Cool and fresh water enters the deep Atlantic between 40°N and 60°N and flows southward (Fig. 2e, f). Below $\approx$4,000 m, Antarctic Bottom Water spreads northward, but it is too warm and too saline.

Figure 3 shows the long-term annual means of sea surface temperature and salinity (SST and SSS, respectively) from present-day run PD, along with their deviation from observations (World Ocean Atlas 2009: Antonov et al. 2010; Locarnini et al. 2010) and from the pre-industrial run PI. While both SST and SSS look realistic (upper row), a

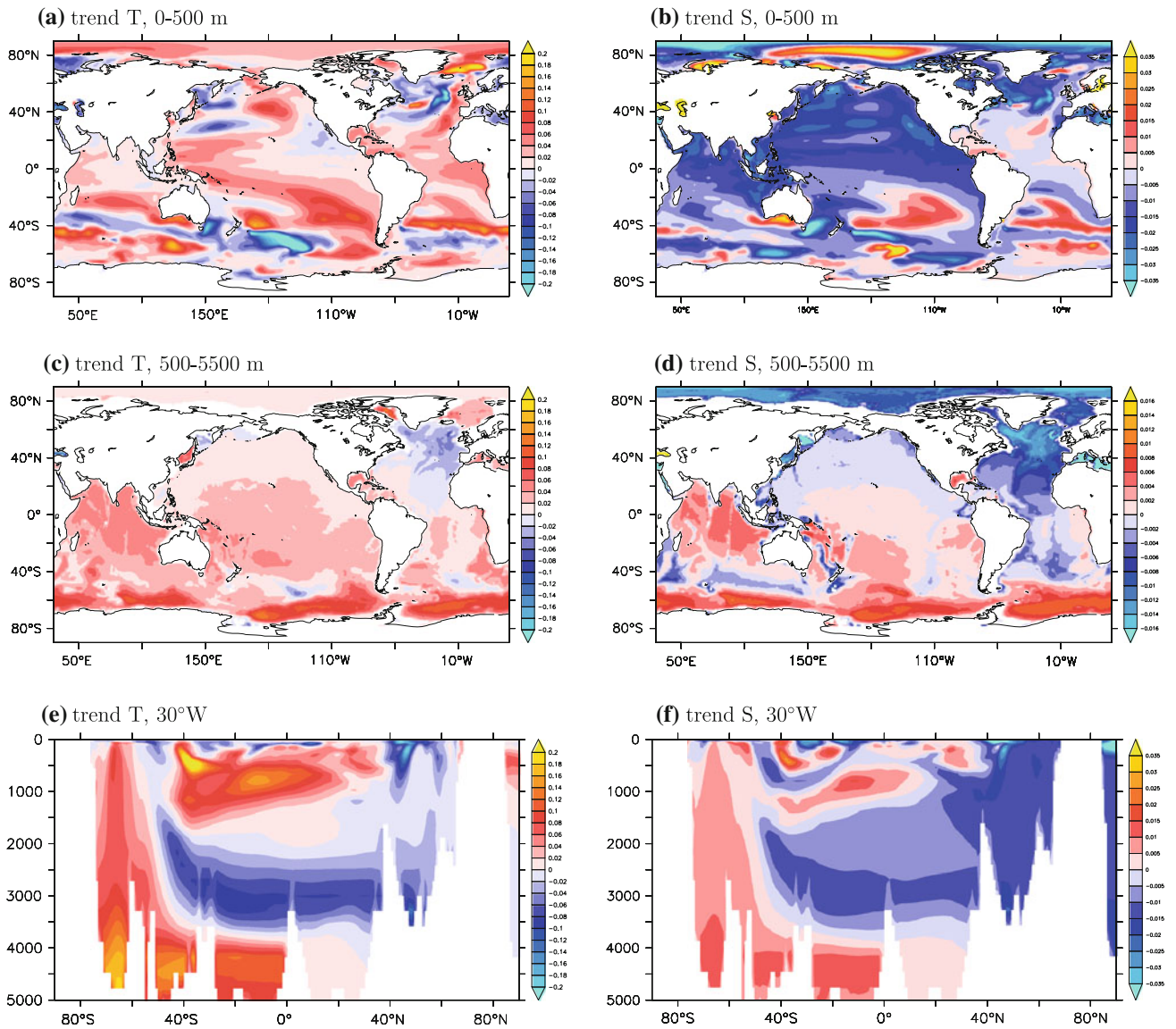


**Fig. 2** Linear trends of temperature (*left*) and salinity (*right*), averaged over the upper 500 m (*upper row*), averaged over depths below 500 m (*middle row*), and along 30°W ind the Atlantic Ocean (*lower row*). The trends are calculated over the last 264 years of the PD run and expressed in K/century (temperature) and psu/century (salinity). Ocean areas shallower than 500 m are left white in **c** and **d**

comparison with observations (middle row) reveals systematic biases.

Most areas equatorward of 40° are too cold, with the exception of the upwelling areas at the eastern boundaries. Both features are common to current climate models (e.g., Randall et al. 2007, their Fig. 8.2). The warm bias at the eastern boundaries is caused by too much solar radiation (see Sect. 3.4.1). With a cold bias of much less than 1 K, EC-Earth is among the warmest climate models. Poleward of 40°, SST is mainly too warm, with the bias reaching 5 K in the Southern Ocean (SO). While a warm bias in the SO is also a common feature in climate models (Randall et al. 2007, their Fig. 8.8), the magnitude found in EC-Earth is clearly exceptional. We investigate this bias in more detail in Sect. 3.3. The SST biases in the Kuroshio and Gulf Stream (GS) regions indicate a wrong position of these currents. They leave the coast too far to the north and are oriented too zonally (see Figure 14 in Sect. 3.6 below). Furthermore, they are too broad, smearing out their warm waters meridionally. This behaviour is characteristic for non-eddy resolving models.

The distribution of SSS bias shows a different pattern. In most regions the surface ocean is too fresh, while the Arctic Ocean is much too salty. The latter is probably a sampling effect: SSS measurements are only done during summer, when the Arctic is covered by a thin layer of fresh melt water. The banded structure of the SSS bias suggests a meridional shift of the main climate zones, but no direct

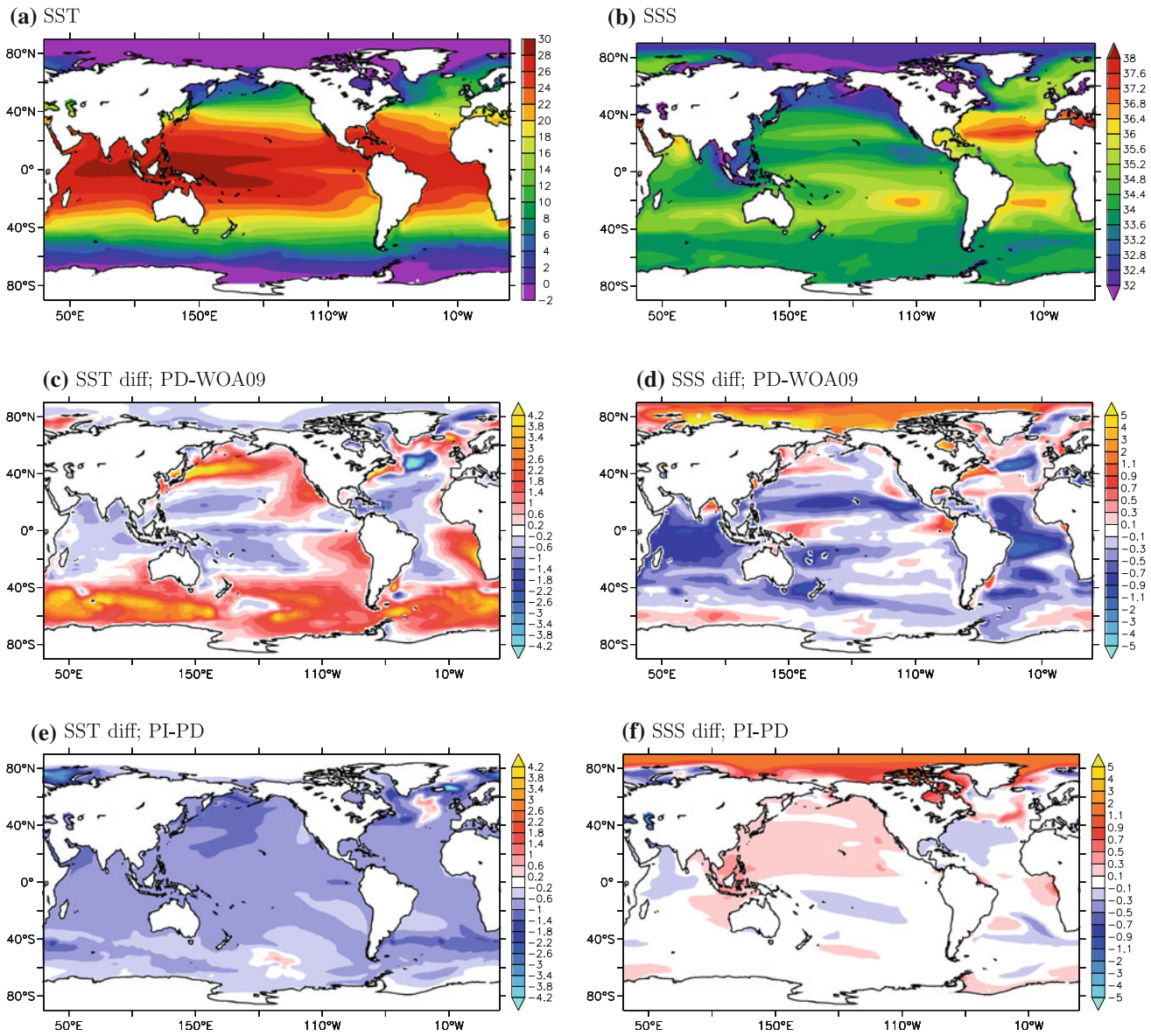


**Fig. 3** SST (*left*; K) and SSS (*right*; psu). *Upper row* long-term annual mean (model years 2326–2425) from the PD run. *Middle row* difference with the WOA09 climatology. This climatology contains annual values, meaning that in the Arctic it is biased towards summer, when measurements are made. This may explain the large SSS bias in the Arctic. *Bottom row* difference between PI (years 1680–1779) and PD (years 2,326–2,425)

correspondence with shifts in wind or wind stress curl is evident (not shown).

Under pre-industrial forcing conditions (Fig. 3, lower row) SST drops more or less uniformly by $\approx$0.8 K, and SSS increases. In both difference fields a banded structure in the SO suggests a meridional shift of the subpolar front. Again this shift cannot be directly linked to a corresponding shift of the belt of westerlies as neither zonal wind stress nor wind stress curl exhibit a clear meridional shift (not shown).

Figure 4 shows temperature and salinity along the section 30°W in the Atlantic Ocean. Temperature and salinity look realistic again (upper row), with warm and salty water entering the interior ocean in the north and a tongue of fresh Antarctic Intermediate Water (AAIW) entering in the south. However, the comparison with WOA09 (middle row) suggests that the region in which the warm and salty water enters the interior in the north is positioned too far to the south, leading to a zone of too warm and salty water extending from the surface at $\approx$40°N to a depth of 1,500 m at 40°S, the southern end of the Atlantic Ocean. To the north of and below this warm and salty water we see a tongue of too cold and fresh water, and even further to the north again too warm

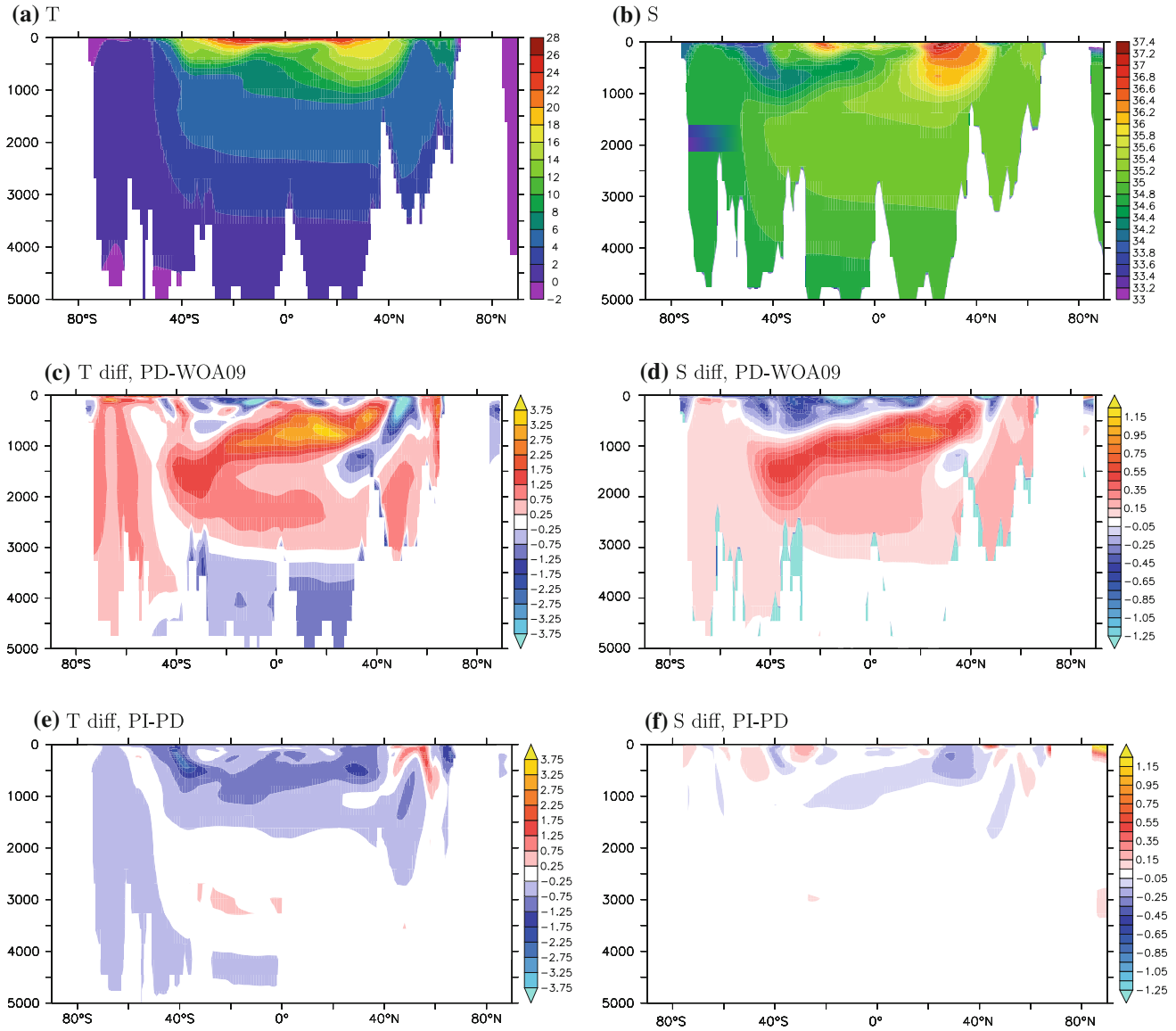


**Fig. 4** As Fig. 3, but for a vertical section along 30°W in the Atlantic Ocean

and salty water. Comparison with the differences at the surface (Figure 3, middle row) reveals that the subsurface structure is the downward extension of a meridional shift of surface SST/SSS. Too warm and too salty water around 60°N and too cold and fresh water at 45°N indicate a southward shift of the main convection sites (see below). The comparison with the pre-industrial run (Fig. 4, lower row) shows a cooling and freshening along the same pathway where the present-day run is too warm and salty. The cooler and fresher surface water at ≈40°N (Fig. 3, lower row) in PI is entering the interior along more or less the same pathway as does the warm and salty water in PD. Thus to a first approximation this pathway is independent of the background climate. The difference pattern also suggests a too shallow return branch of the meridional overturning circulation (MOC) in the model (see Sect. 3.7).

Figures 5 and 6 give some more insight into the vertical structure of the model ocean. A tongue of too warm and too saline water is seen to move southward and gain depth in the Atlantic Ocean. This water apparently originates from the outflow of the Mediterranean Sea and produces the large southward-descending structure that we saw in the middle panels of Fig. 4. This suggests Mediterranean outflow water to be the source of the bias. It may be too warm and salty, not mix enough with the surrounding water in the Atlantic, or the outflow may be too strong. In Sect. 3.6 we show that the latter is the case.

At all levels the water close to Antarctica is too warm and too saline. Below 1,000 m the temperature bias (Fig. 5)

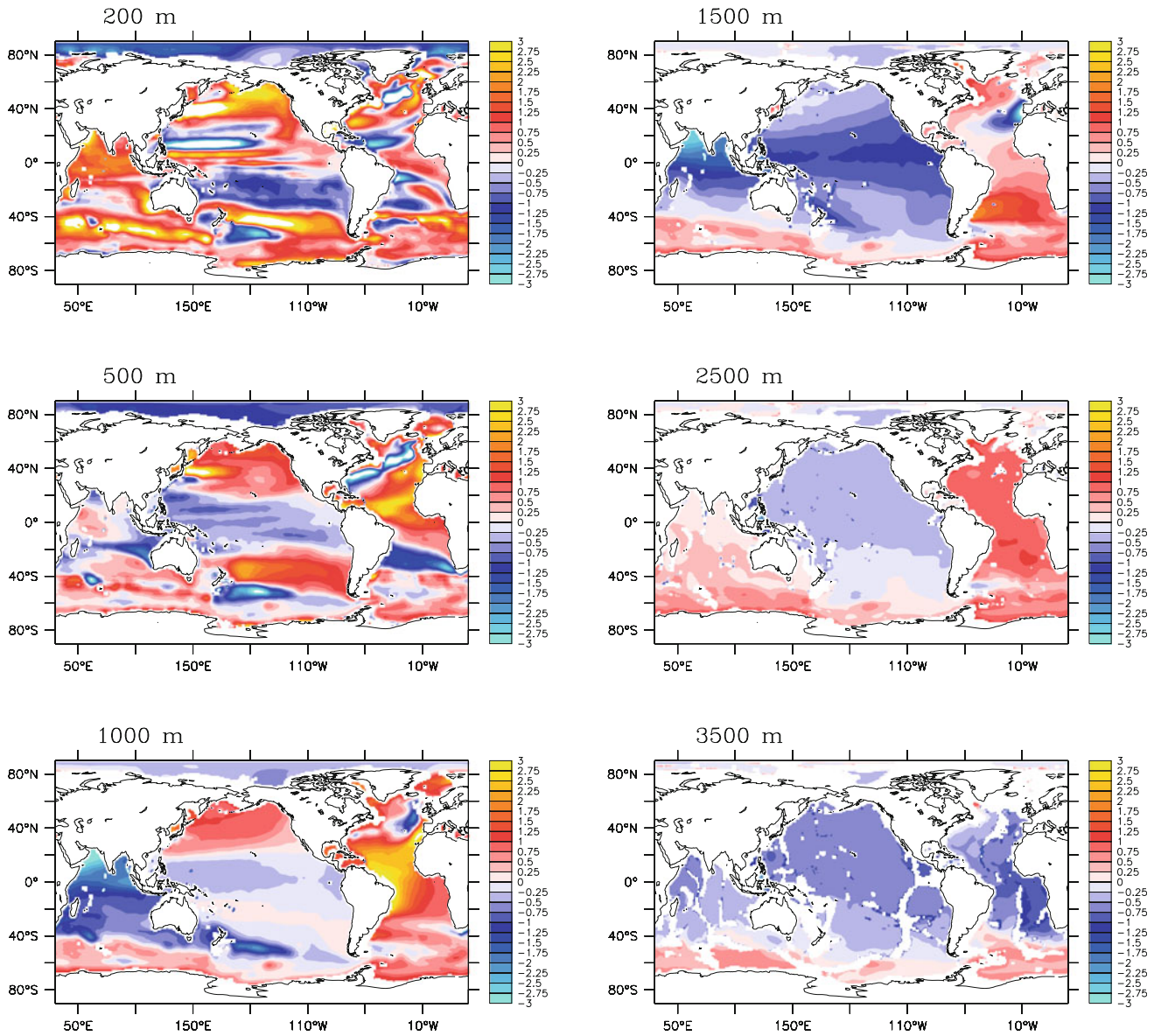


**Fig. 5** Difference (in K) between modelled temperature (PD run) and the WOA09 climatology at different depths as indicated on the *plots*. Model values have been averaged over 100 years (2326–2425)

becomes smaller away from Antarctica and changes sign to become negative in the interior of the basins. This negative bias is largest in the Pacific. The salinity bias (Fig. 6) has a different pattern. At greater depths it is nearly everywhere positive and has a maximum roughly along the northern edge of the ACC. The pattern at 1,500 m depth even suggests that the too salty Mediterranean outflow finds its way into the Southern Ocean. At this depth it reaches the northern edge of the ACC near 40°S (Fig. 6), from where the area of maximum bias extends eastward into the Indian Ocean, closely following the path of the model ACC (not shown).

A good indicator for the strength of convection is the mixed layer depth (MLD) (Fig. 7a). EC-Earth simulates the deepest mixed layer (ML) south of Greenland and south of Svalbard in the Greenland Sea. In both areas, mean modelled MLD exceeds 1 km, with individual years reaching 2 km (not shown). This compares well with existing observations (e.g., Lavender et al. 2002, Wadhams et al. 2004, Morawitz et al. 1996). However, compared to observations the deep convection regions in the model are slightly shifted to the southeast in the Labrador Sea, and to the north in the Greenland Sea. The shift in the Labrador Sea may be related to the sea ice, which extends too far south (see Sect. 3.5). As Fig. 7a shows, a deep ML corresponds to a positive SST error. This correspondence is confirmed by Fig. 7b, which shows that deeper MLs in the PI run tend to correspond with warmer SSTs.

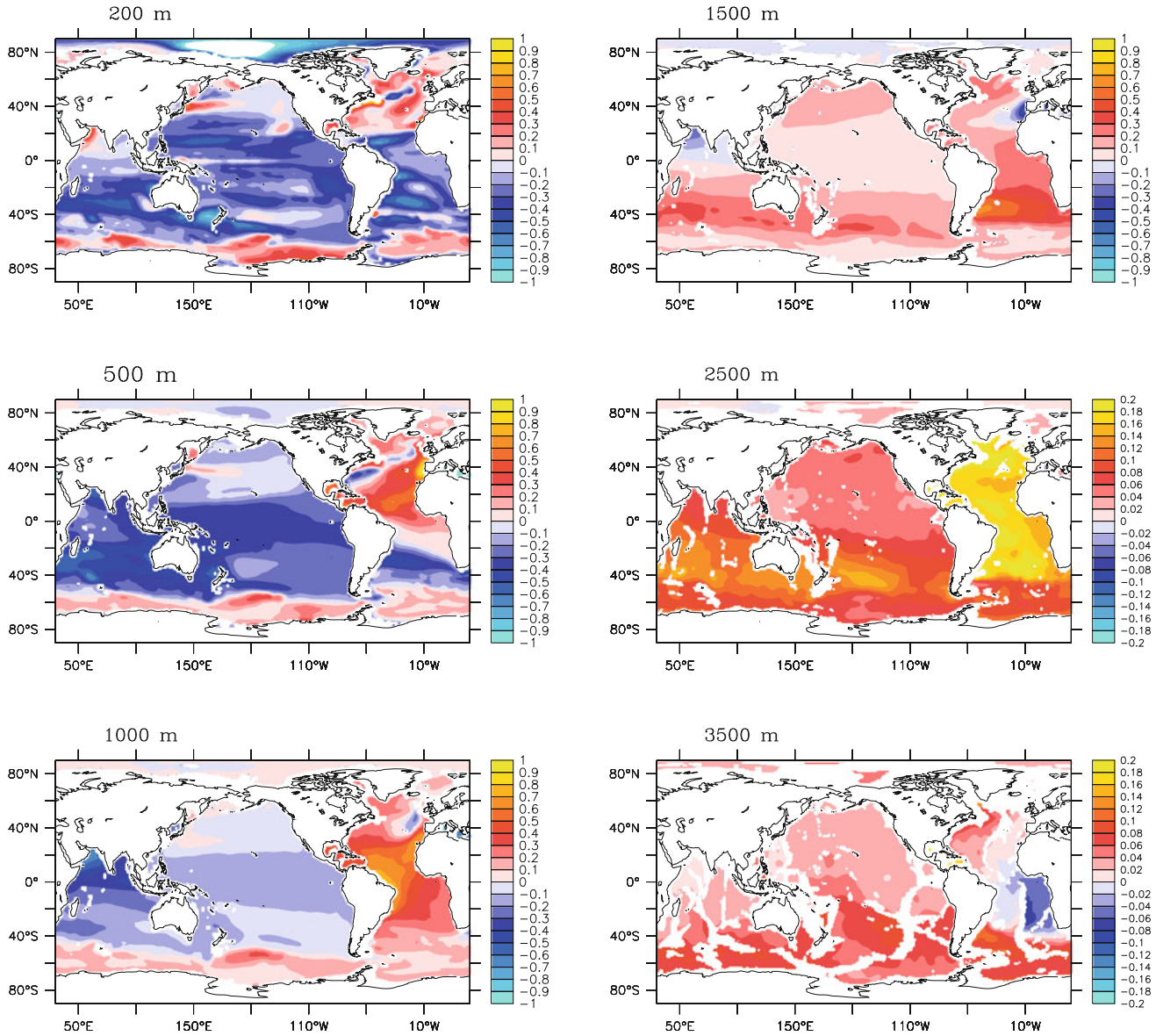


**Fig. 6** As Fig. 5, but for salinity (in psu). Note the change in plotted range at the two lowest levels

### 3.3 SST bias in the Southern Ocean

As shown in Fig. 3c, modelled SST in the SO is much too high. Inspection of the atmospheric circulation (not shown) does not reveal large errors in the atmosphere, suggesting an oceanic origin of the error. This suspicion is backed by the fact that during the stand-alone spin-up of the ocean model the diagnosed heat flux is anomalously cooling this area (not shown). On the other hand solar heat flux into the SO is consistently too high (see Fig. 10h below). This excess heating is largely, but not completely, compensated by too large a cooling by the SST-dependent fluxes of latent and sensible heat and longwave radiation (see Figs. 9 and 10b, d, f, j). In a way the coupled model recognizes the fact that SST is too high and tries to compensate by excessive cooling.

Fig. 4c shows that in the SO the largest temperature error is confined to an area close to the surface. This suggests incoming heat from the atmosphere not penetrating deep enough, or, in other words, a too shallow mixed layer. This is confirmed by Fig. 8, which shows a comparison between MLD derived by Dong et al. (2008) from 5 years of Argo float data, and model data. While the geographical pattern of MLD is well captured by the model, its magnitude is severely underestimated. This is true for both seasons. The underestimation of MLD occurs despite the fact that the wind stress is overestimated in the SO (see Fig. 10l, n below). Excess wind stress should favour a deep ML.

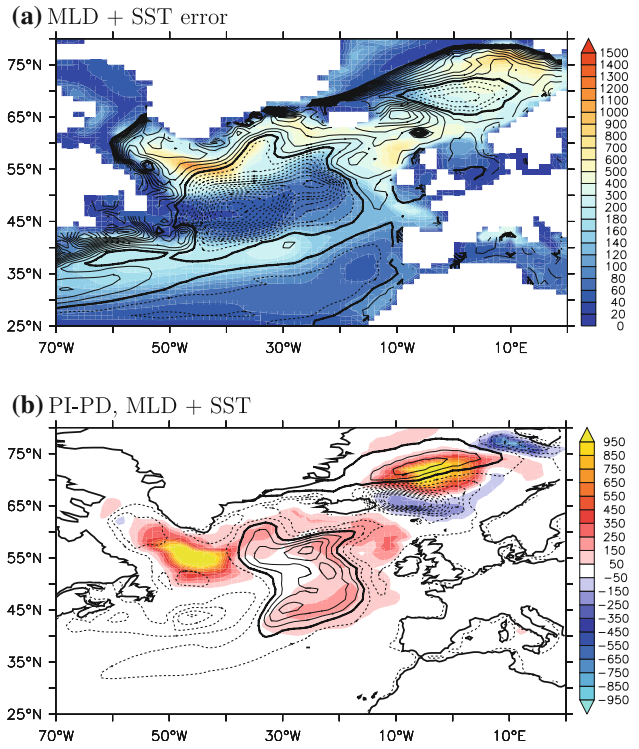


**Fig. 7** **a** Climatological March MLD (m) in PD (*colors*), with March SST error (model—ERA-40; CI = 0.5 K, *negative dashed*) superimposed. **b** Difference in climatological March MLD (m) between PI and PD. Superimposed is the corresponding SST difference (CI = 0.5 K)

Recently, Huang et al. (2011) identified wave-turbulence interaction (Langmuir circulation inducing turbulence) as a main mechanism lacking in TKE-type ML models. This mechanism and some other improvements in the TKE scheme have been introduced into NEMO version 3, which will be used in the next EC-Earth version (v3, see Sect. 6). First results, both from ocean-only and from coupled integrations, show an improvement in modelled SSTs (not shown).

The comparison in Fig. 8 needs one word of caution. Dong et al. (2008) provide four different estimates of MLD. The one displayed in Fig. 8 is based on a 0.03 kg/m$^2$ density difference, while the model uses a difference of only 0.01 kg/m$^2$ to diagnose MLD. However, the model also provides for a measure of MLD directly obtained from the TKE scheme, and both measures do not differ by more than a few tens of metres. On the other hand, the other three estimates obtained by Dong et al. (2008), although different, are all much deeper than any of the two model-based estimates. So while the actual numbers in Fig. 8 might not be directly comparable, modelled MLD is certainly too small.

### 3.4 Surface heat fluxes

In this section we focus on air-sea fluxes of heat and momentum (i.e., wind stress). All components of these

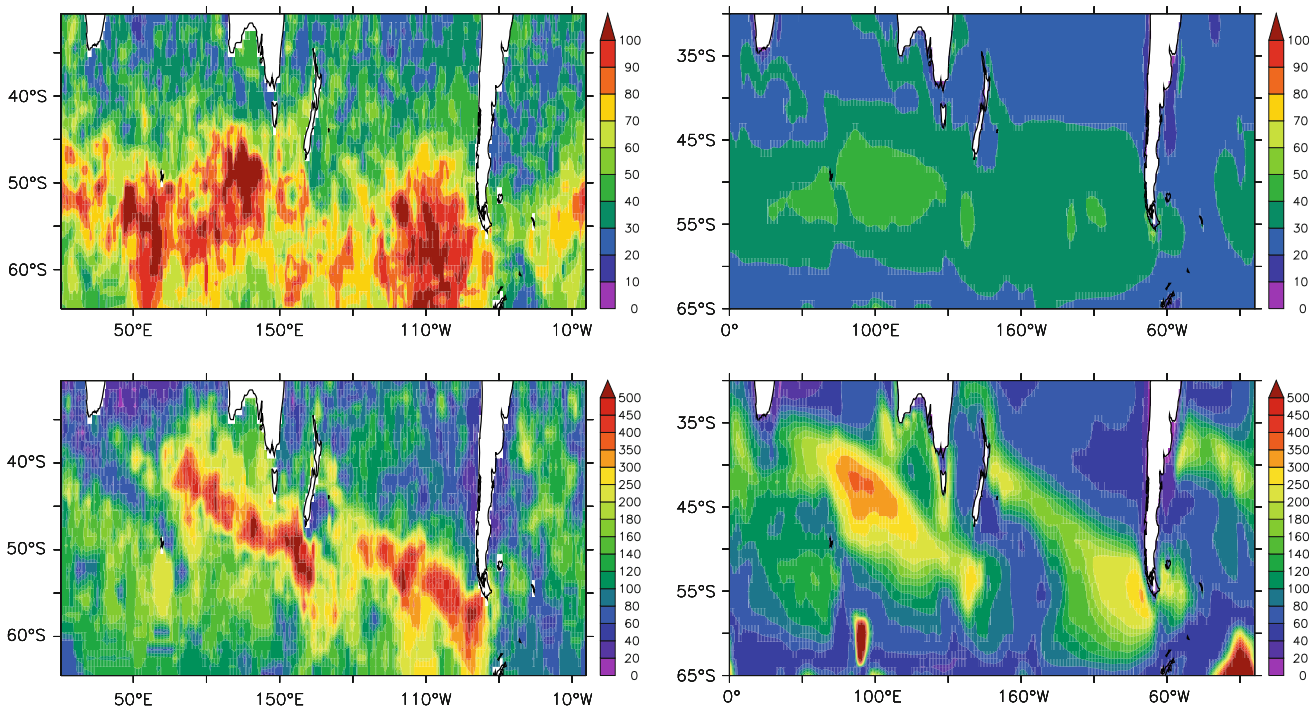


**Fig. 8** MLD (in m) in the SO in March (*upper row*) and September (*lower row*) from the climatology of Dong et al. (2008) (*left*) and from PD run (*right*). Note the *different color bars* for March and September

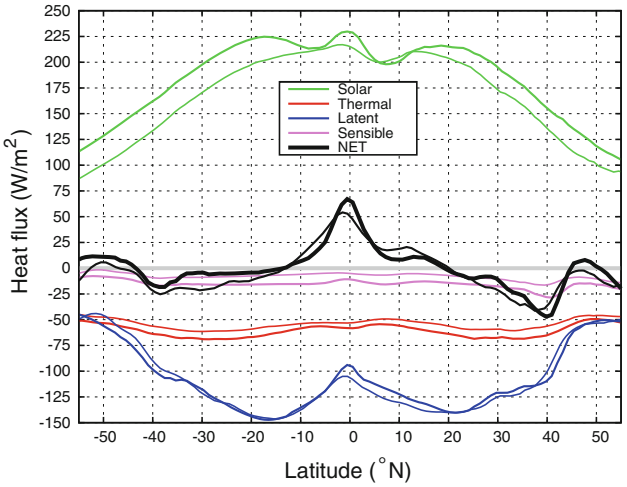


**Fig. 9** Zonally-averaged air-sea heat flux components from EC-Earth (PD run) (*thick lines* period = 1980–2005) and the NOC1.1 adjusted climatology (Grist and Josey 2003) (*thin lines*)

fluxes are computed by IFS using NEMO prognostic SST and transmitted back to NEMO, which uses them as surface boundary conditions for the vertical continuity of momentum, heat, and salt. To asses the "realism" of these surface fluxes, we compare heat fluxes and evaporation to their counterparts from the so-called NOC1.1a adjusted climatology (Grist and Josey 2003). Wind stress is compared to both the Scatterometer Climatology of Ocean Winds (SCOW; Risien and Chelton 2008) and the ERA-interim reanalysis (Simmons et al. 2007). We use the convention that positive fluxes are directed downward, i.e., entering the ocean.

### 3.4.1 *Net heat flux and evaporation*

The solar radiation (shortwave) differs from the other three components of the net heat flux in that it is penetrative and does not depend on the SST. On a zonal average basis, when compared to NOC1.1a (Fig. 9), EC-Earth significantly overestimates the input of solar radiation, especially at extra-tropical latitudes of both hemispheres (about +25 W/m$^2$ for SH and +20 W/m$^2$ for NH) and at the equator (+20 W/m$^2$).

The excess of solar radiation in the southern hemisphere (SH) is uniformly "spread" south of 40°S (Fig. 10h). This contributes to the excess of net heat flux input under these latitudes as shown by Fig. 9 (black curve), which, in turn, is likely contributing to the warm southern bias discussed in Sect. 3.3.

Between 15° and 45° in both hemispheres, the excess of solar radiation is particularly pronounced over eastern boundary regions with values locally exceeding 70 W/m$^2$. This last feature is due to a poor representation of low-level stratus and stratocumulus clouds in the regions of subsidence of the Walker cell. This is a general feature of atmosphere models and has been described for IFS by Gibson et al. (1997). Interestingly, these regions also correspond to regions of pronounced warm biases as seen in Fig. 3c.

Globally, heat loss linked to the thermal (longwave) radiation is slightly overestimated by EC-Earth (Fig. 9). Figure 10j suggests that the disagreement with observations is more pronounced in the same eastern boundary regions that are affected by the excessive solar input. As these regions are too warm, they emit too much longwave radiation. At the same time the cloud cover is too low, reducing the downwelling longwave radiation. Both mechanisms work in the same direction and lead to an overestimation of the heat loss due to the longwave radiation.

Evaporation/latent heat flux is of primary importance since it stands as the major heat loss contributor (Fig. 9) for the ocean and impacts both the heat and freshwater budget of the ocean. Figure 9 shows that the zonally-averaged latent heat flux in EC-Earth is in a rather good agreement with NOCS1.1a estimates except at the equator and in the northern tropical band (0 to 20°N), where the associated heat loss is underestimated by about 10 W/m$^2$. Differences to the climatology shown in Fig. 10d suggest that this lack of evaporation, while affecting all three main oceans, is more pronounced in the central and eastern Pacific. In the North Atlantic, evaporation is underestimated along the whole path of the North Atlantic Current (NAC), where it corresponds to an excess of heat input in the order of +80 W/m$^2$. Interestingly, the opposite feature is observed in the northern Pacific in the Kuroshio region, where an excess of evaporation locally induces a heat loss anomaly of about −80 W/m$^2$. The same Kuroshio region is also subject to a remarkably high anomaly of sensible heat loss of about −50 W/m$^2$ (Fig. 10f). The biases in heat flux reflect the SST biases found in the same areas (Fig. 3c) and, like those, have their origin in a wrong position of the Kuroshio and GS (Sect. 3.6). Note that these two "western boundary particularities" have a direct impact on net heat flux (Fig. 10b), but cancel each other in the zonal average (Fig. 9).

The zonal averages of each heat flux component (Fig. 9) reveal that the excess of solar radiation is partly balanced by the excess of both thermal radiation and sensible heat flux. The whole SO suffers from an excessive input of heat directly attributable to the excessive solar radiation. Another problematic region is the eastern equatorial Pacific where both excessive solar radiation and insufficient evaporation yield an excess heat flux of the order of 50 W/m$^2$ (Fig. 10b). This is even visible in the zonally averaged net heat flux, which shows an anomaly of roughly +20 W/m$^2$ at the equator. The most problematic region of the

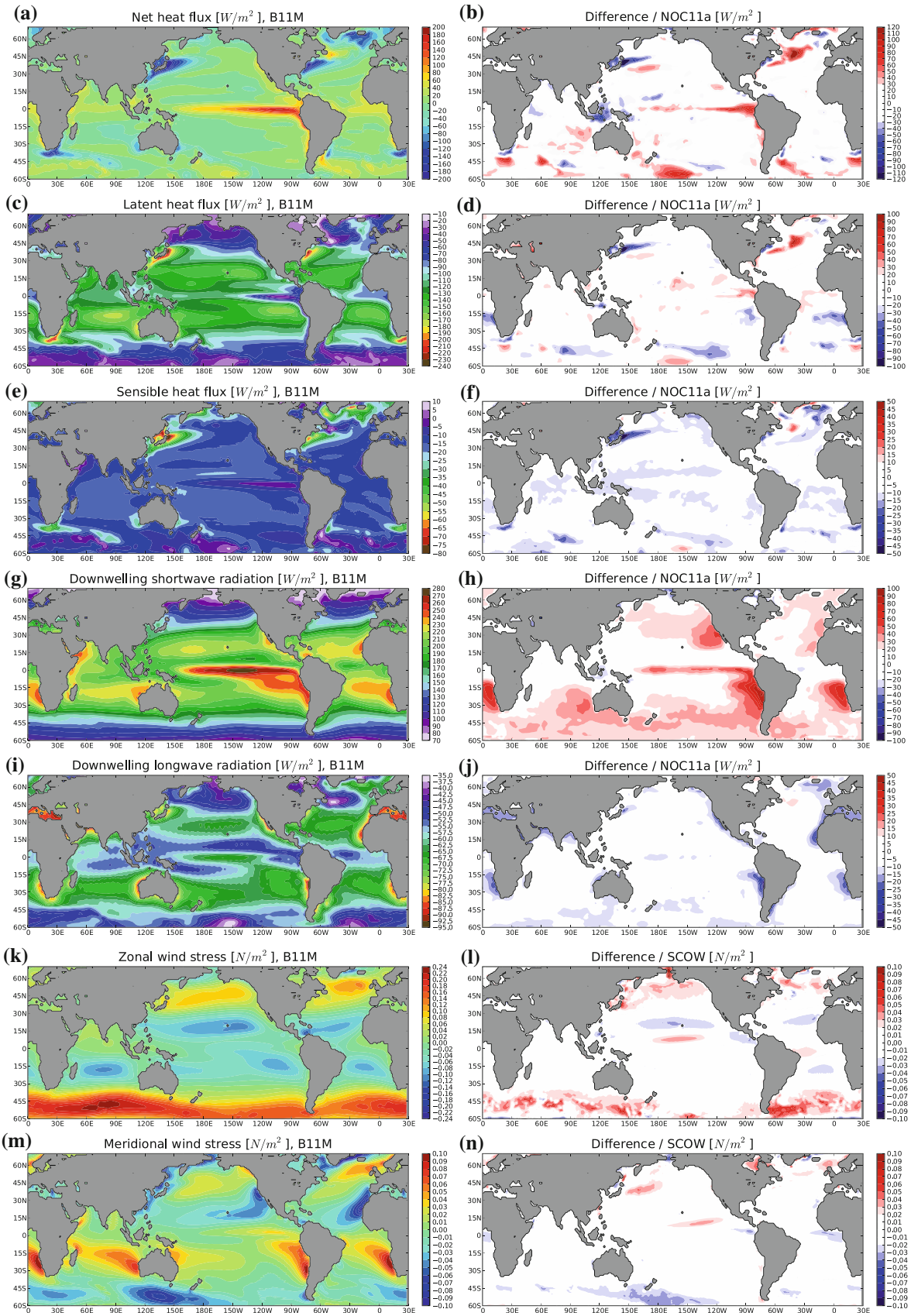
(a)
Net heat flux [$W/m^2$ ], B11M
(b)
Difference / NOC11a [$W/m^2$ ]
(c)
Latent heat flux [$W/m^2$ ], B11M
(d)
Difference / NOC11a [$W/m^2$ ]
(e)
Sensible heat flux [$W/m^2$ ], B11M
(f)
Difference / NOC11a [$W/m^2$ ]
(g)
Downwelling shortwave radiation [$W/m^2$ ], B11M
(h)
Difference / NOC11a [$W/m^2$ ]
(i)
Downwelling longwave radiation [$W/m^2$ ], B11M
(j)
Difference / NOC11a [$W/m^2$ ]
(k)
Zonal wind stress [$N/m^2$ ], B11M
(l)
Difference / SCOW [$N/m^2$ ]
(m)
Meridional wind stress [$N/m^2$ ], B11M
(n)
Difference / SCOW [$N/m^2$ ]

◀ **Fig. 10** *Left* time average (1980–2005) of each surface flux component as computed by EC-Earth (PD run). *Right* corresponding differences to the relevant climatology (EC-Earth—climatology). Positive fluxes are directed downward into the ocean

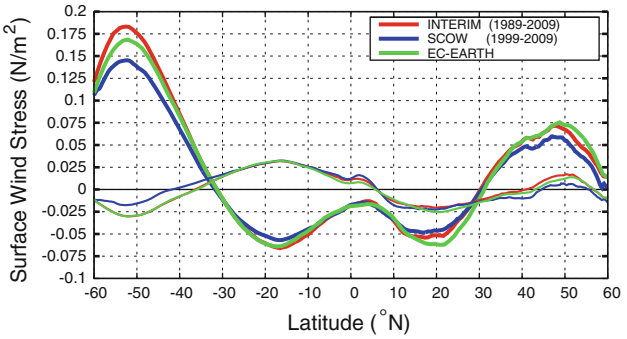


**Fig. 11** Zonally-averaged surface wind stress components from EC-Earth (PD run), ERA-interim (Simmons et al. 2007) and the SCOW climatology (Risien and Chelton 2008). Zonal component (*thick lines*) and meridional component (*thin lines*)

northern hemisphere (NH) in terms of net heat flux is the mid-latitude central Atlantic Ocean, where heat and freshwater losses are significantly underestimated along the whole path of the NAC. This is a direct consequence of the wrong position of this current.

### 3.4.2 Wind stress

Globally, the wind stress from EC-Earth is in rather good agreement with both the SCOW and the ERA-interim climatologies. Large differences only occur in the ACC (Antarctic Circumpolar Current) region, where the model significantly overestimates the zonal stress with respect to SCOW (see Figs. 10l, n, 11), but underestimates it compared to ERA-interim (Fig. 11). Both SCOW and ERA-interim are modern, state of the art products. That they bracket the values simulated by EC-Earth shows that the model is compatible with our present knowledge about the wind stress in the SO. Fig. 10l shows that the regions of excessive wind stress are mainly located in the southern Atlantic and Pacific. They are particularly pronounced south-east of both South America and Australia. This suggests that the intensity of the wind stress cannot be blamed for the weak ACC strength (see Sect. 3.6).

To a smaller extent, mid-to-high latitudes of the NH also suffer from an overestimation of the zonal wind-stress, particularly in the northern Pacific. The stronger wind-

**Fig. 12** Sea ice thickness (in m) averaged over 100 years of PD run. **a**, **b** Arctic ice thickness in March and September, **c**, **d** Antarctic ice thickness in March and September. Note that the size of the intervals changes at 1 m

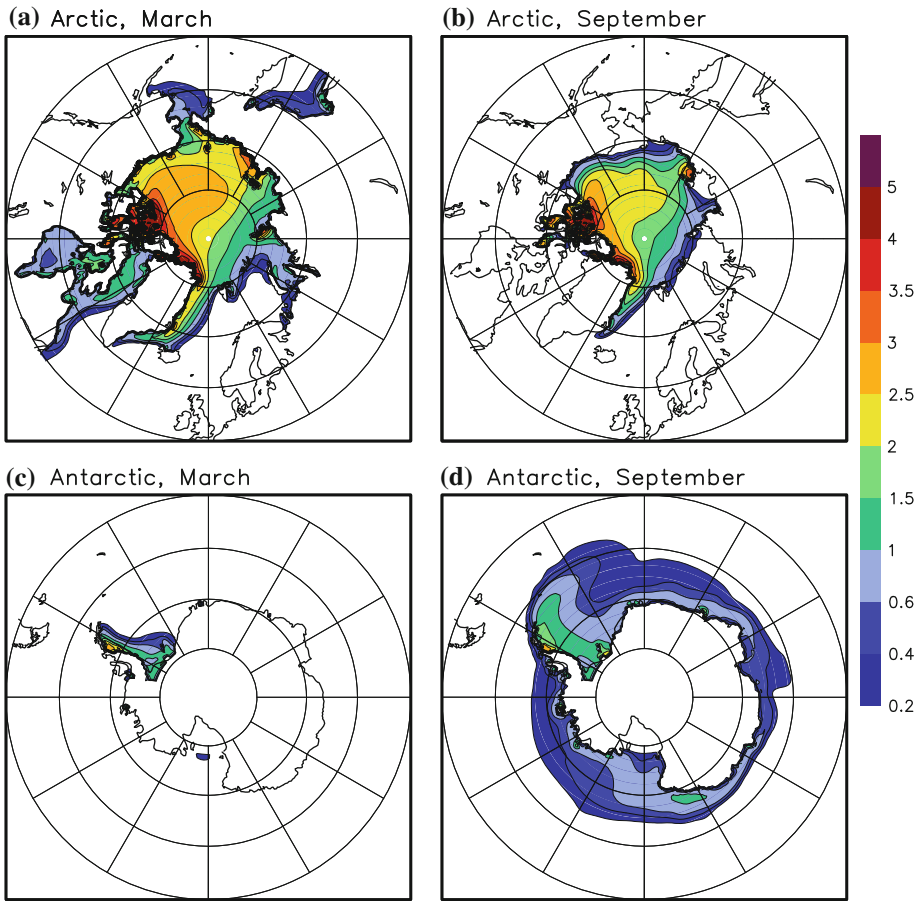

driven circulation in the northern Pacific could lead to the enhancement of the Kuroshio current which could partly explain the excessive turbulent heat loss found on the Kuroshio path (see 10d, f).

### 3.5 Sea ice

As an interface between ocean and atmosphere, sea ice controls most of the heat, momentum and fresh water transfers in sea ice covered regions, The ice effectively reflects the incoming solar radiation, but acts almost as a perfect black body radiator for the outgoing terrestrial radiation. Melting and freezing processes of sea ice and its export through Fram Strait affect the freshwater balance of the Arctic Ocean. The large and strongly varying export of sea ice through Fram Strait has an important impact on the deep water formation in the North Atlantic Ocean (e.g., Dickson et al. 1988; Haak et al. 2003; Koenigk et al. 2006). As shown in Sect. 3.7, EC-Earth shows a similar impact of Fram Strait sea ice export on convection and thus deep water formation.

Figure 12 shows the mean sea ice thickness in the Arctic and Antarctic in March and September in PD. The ice thickness distribution in the Arctic fits well to available observations and estimates but is overestimated at the Siberian coast. Due to missing comprehensive data, we rely here on the established view of recent climate ice thickness, based on various observations and analysis methods (e.g., Belchansky et al. 2008; Rothrock et al. 2003). The ice in EC-Earth is thickest north of Greenland and the Canadian Archipelago with up to 5 m in late winter. In the Central Arctic, ice thickness varies between 2 and 3 m. The seasonal cycle of ice thickness in the Central Arctic and the Beaufort Gyre is relatively small. The ice in late summer/early autumn is less than a meter thinner than in late winter/early spring.

The ice extent is comparably well simulated with for instance a partly ice-free Barents Sea during winter. In winter the ice extends slightly too far south and east along the east coast of Greenland and too far south in the Labrador Sea. The summer sea ice extent in the European Arctic sector fits well to satellite observations, but too much ice is left at the Siberian coast. Here, the ice is too thick both in summer and winter, which is a common problem of coupled climate models (e.g., DeWeaver and Bitz 2006; Goosse et al. 2002; Koenigk et al. 2006).

In the Antarctic, sea ice thickness seems to be generally slightly underestimated, and ice extent is underestimated in the SH summer. This is probably mainly due to the warm bias in the ocean around Antarctica (Sect. 3.2).

The annual cycles of ice extent and ice volume in both hemispheres are shown in Fig. 13a, b. The annual cycle of the Arctic ice extent is well simulated in EC-Earth

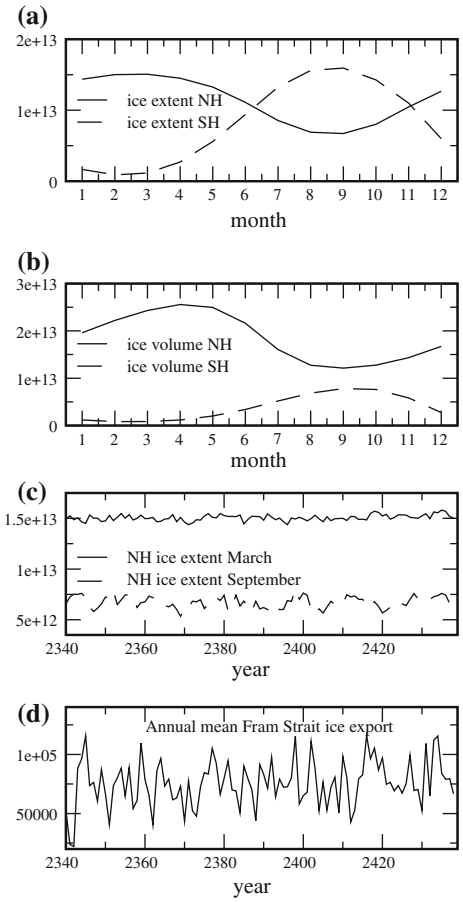


**Fig. 13** Sea ice characteristics obtained from 100 years of the PD run. Northern and Southern Hemisphere mean annual cycles of **a** ice extent ($m^2$) and **b** ice volume ($m^3$). **c** Time series of Northern Hemisphere ice extent ($m^2$) in March and September, and **d** annual mean Fram Strait ice export ($m^3/s$)

**Table 2** Arctic Sea ice extent and standard deviation (in $10^6$ $km^2$) in EC-Earth PD and satellite observations (Cavalieri et al. 2008)

| | | PD model | Observations | |
|---|---|---|---|---|
| | | 2340–2439 | 1995–2005 | 1978–2009 |
| Extent (min/max) | March | 15.1 (14.4/15.8) | 15.0 (14.8/15.3) | 15.2 (14.5/15.9) |
| | September | 6.7 (5.3/7.9) | 6.3 (5.6/7.7) | 6.5 (4.3/7.7) |
| SD | March | 0.29 | 0.18 | 0.32 |
| | September | 0.57 | 0.37 | 0.82 |

compared to satellite observations (Cavalieri et al. 2008). The ice extent is slightly overestimated during summer due to too much ice at the Siberian coast (Table 2).

Sea ice extent in the Antarctic in EC-Earth fits well to observations at the end of the SH winter, but underestimates the sea ice minimum in February by almost 2 million $km^2$. Minimum and maximum occur in the same months as in observations, but the annual cycle is too pronounced.

The maximum of Arctic sea ice volume peaks 1–2 months later than the ice extent. While sea ice already melts at the ice edges, it still grows in the Central Arctic. Between June and August, ice volume rapidly decreases, and its minimum occurs simultaneously with that of the extent in September. Thereafter, ice volume grows almost linearly until April. Average maximum and minimum Arctic ice volumes are 25,600 and 12,500 $km^3$, respectively. This compares well with estimates of Belchansky et al. (2008) of about 22,000 and 12,000 $km^3$.

Sea ice volume in the SH varies between 870 $km^3$ in February and 8500 $km^3$ in September in EC-Earth. Sea ice volume estimates based on observations for the Antarctic are even more uncertain than for the Arctic. However, we can estimate sea ice volume based on ice thickness and ice concentration observations by Worby et al. (2008) to about 1,600 $km^3$ and 11,000 $km^3$ in summer and winter, respectively.

Figure 13c and Table 2 show interannual variations of Arctic sea ice extent. Modelled variability appears to be within the range of observational estimates.

The Fram Strait sea ice export shows a high interannual variability (Fig. 13d) with annual mean values between 20,000 $m^3/s$ and 130,000 $m^3/s$. The mean value is 75,500 $m^3/s$. This is in very good agreement with observational estimates of for instance Vinje (2001) and Kwok et al. (2004), who found values of 92,000 $m^3/s$ and 70,000 $m^3/s$, respectively.

### 3.6 Major ocean current systems and transports through straits

We assess the ability of EC-Earth to reproduce the major ocean circulation patterns. Figure 14 shows the mean current pattern at 25 m depth (model level 3) for January and July. Generally, the highest values are found in the

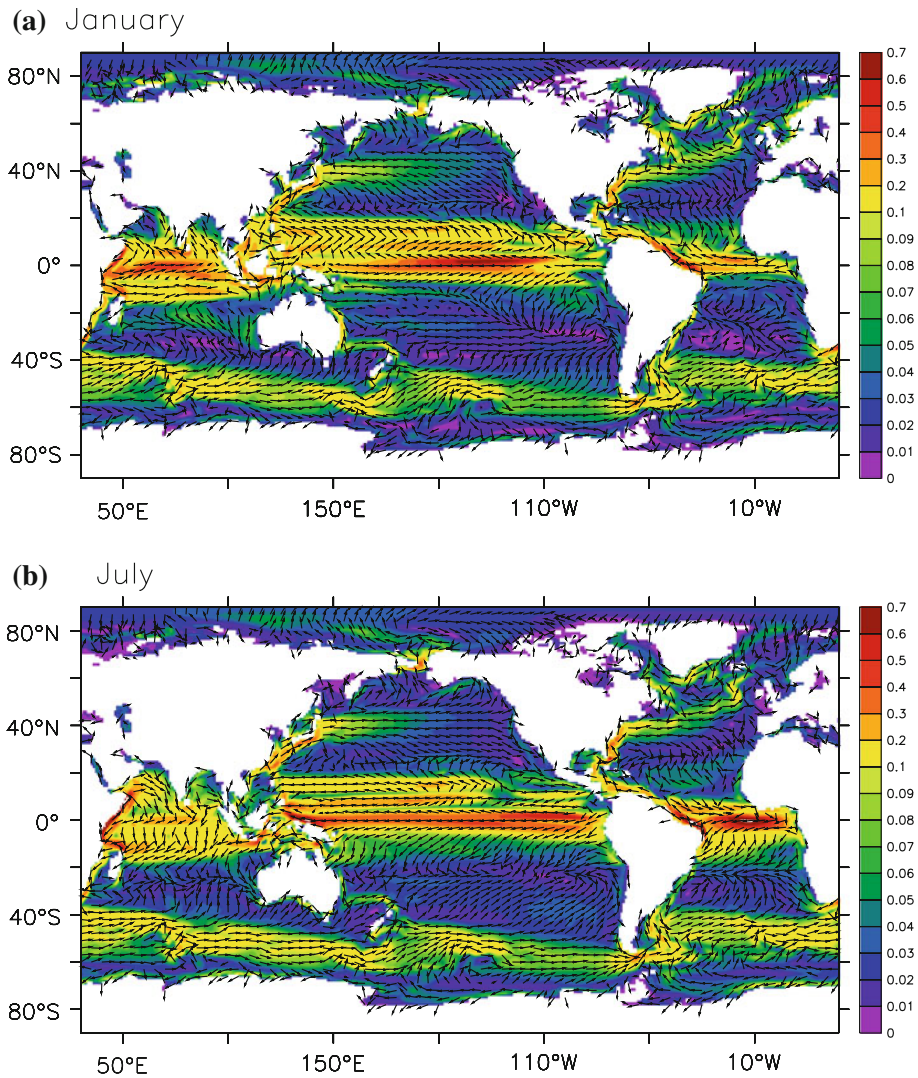


**Fig. 14** Climatology of modelled ocean currents (in m/s) at 25 m depth for January and July. *Colors* denote the magnitude as derived from monthly-mean u and v components. Note the break in the color scale at 0.1 m/s. The *arrows* have unit length and denote the direction only

equatorial regions. The equatorial Atlantic is dominated by the westward flowing Southern Equatorial Current and its continuation, the North Brazil Current. This current system is present throughout the year, but strongest during boreal summer. North of this, we find the weaker Equatorial Counter Current, which is present in boreal summer only. These two currents reach down to about 100 m. The North Equatorial Current is hardly present in EC-Earth.

In the Equatorial Pacific we have a more cleancut equatorial current system, with westward flowing Northern and Southern Equatorial currents (the southern being the strongest) and in between them the east flowing Equatorial Counter Current. The whole current system is persistent throughout the year, but modified during El Niño/La Niña events (see Sect. 3.9). Also the Indian Ocean has an equatorial current system, which is modified by monsoon-driven currents due to the proximity of the Asian continent.

In all three ocean basins the equatorial current systems display a clear annual cycle. For instance, the currents reverse direction in the area of the North Brazil Current and along the Somalian coast and around the Indian subcontinent between January and July, and the convergence areas between the equatorial currents and the subtropical gyres move northward during the same time.

Poleward of the equatorial current systems, EC-Earth reproduces the subtropical gyre circulations in the Northern and Southern Atlantic, the Northern and Southern Pacific and in the Indian Ocean. We see westward intensification, which causes well-known currents like the GS and Kuroshio currents reaching down to a depth of a few 100 m, and we see the broader and slower return flows. The positions of the GS and Kuroshio are not correct, as already mentioned in Sect. 3.2. They follow the coast northward and do not leave it near Cape Hatteras (GS) or west of Kyushu island (Kuroshio). In the Atlantic this causes the southward flowing Labrador Current to deflect eastward at the latitude of Newfoundland instead of following the coast southward, leading to the cold SST bias around 40°W, 45°N (Fig. 3c). The Kuroshio only turns eastward as far north as Hokkaido island, leading to too warm SST in the northern North Pacific (Fig. 3c).

The subtropical gyre circulations are persistent throughout the year without much seasonal variation. In the Atlantic, we find further north the Subpolar and Polar gyres, respectively south and east of Greenland. The Subpolar Gyre does not reach far enough south (see above). In the SO we have the ACC at $\approx 60°$S, representing a connection between the world oceans and therefore an important part of the global thermohaline circulation.

Having shown that the EC-Earth model is able to reproduce the main features of the global circulation in a qualitative sense, we now turn to a more quantitative evaluation by comparing observation-based and modelled estimates of the mass transports at selected cross sections. In Table 3 we compare mean values from the PD and PI runs with observational estimates.

Drake Passage, between the southern tip of South America and Antarctica, is the best monitored section of the ACC. The modelled volume transport is slightly above 100 Sv in PI and nearly 110 Sv in PD. The annual cycle has an amplitude of $\approx 5$ Sv, with higher values in austral winter than during summer. Estimates based on observations are around 134 Sv, but with a large uncertainty of up to 27 Sv (Cunningham et al. 2003). Thus the modelled estimate is quite low, but not necessarily unrealistic.

This underestimation is surprising as a relatively coarse-resolution model like our present ORCA1 configuration ($1° \times 1°$) should overestimate the ACC strength due to a too weak form drag (eddies induced by bathymetry, Gnanadesikan and Hallberg 2000) when driven with realistic wind stress. As we saw in Sect. 3.4.2, the modelled wind stress in the SO is compatible with our current knowledge and even is too high when we compare with the SCOW

**Table 3** Estimated volume transports (in Sv) for runs PI, PD, and from observations. NAC denotes a section through the North Atlantic Current at 35°W, meridionally extending from 37°N to 53°N. The PI and PD values are averages over the last 100 years, except for AMOC, which is averaged over the last 250 years of the respective run

| Section | | PI | PD | Observation | Reference |
|---|---|---|---|---|---|
| Drake Passage | Annual | 103 | 109 | 134 | Cunningham et al. (2003) |
| Indonesian | Jan | 7.2 | 7 | | |
| Throughflow | Jul | 20.2 | 16 | | |
| | Annual | 13.3 | 12.6 | 15 | Sprintall et al. (2009) |
| Florida Strait | Annual | 19.4 | 19.5 | 25 | Hamilton et al. (2005) |
| Bering Strait | Annual | 1.3 | 1.5 | 0.8-1 | Woodgate et al. (2006) |
| Strait of Gibraltar | Inflow | 1.77 | 1.78 | 0.78 | Tsimplis and Bryden (2000) |
| | Outflow | 1.73 | 1.74 | 0.67 | |
| NAC | Annual | 40.8 | 44.5 | 51 | Yaremchuk et al. (2001) |
| AMOC (30°N) | March | 14.2 | 11.8 | $\approx 14$ | Kanzow et al. (2010) |
| | Jul | 19.4 | 16.3 | $\approx 21$ | |
| | Annual | 16.5 | 14.5 | $18.7 \pm 2.1$ | |

climatology. Too high a wind stress would lead to an even higher ACC strength.

Barnier et al. (2007) performed a series of ocean-only integrations using NEMO in the high-resolution ($^1/_4°$) ORCA025 configuration. They find Drake Passage transports varying between 115 and 155 Sv. However, the last value was obtained from a run in which the density structure (T and S) in the polar areas was restored to observations. This points to the density structure in the SO having an important impact on Drake Passage transport, and Figs. 4, 5 and 6 confirm that NEMO has problems in maintaining a realistic density structure there.

The Indonesian Throughflow between Australia and Java is well-monitored and also an important part of the global thermohaline circulation. The modelled estimate is around 13 Sv with a large annual cycle of around 7 Sv in January and around 19 Sv in August. A recent observation-based estimate is around 15 Sv (Sprintall et al. 2009) with a very asymmetric annual cycle (maximum in July, minimum in October) of ±3 Sv and an uncertainty of ±4 Sv.

Another important strait is Bering Strait, through which relative fresh water from the North Pacific enters the Arctic and ultimately the North Atlantic. This fresh water transport partly compensates the loss of fresh water from the Atlantic through atmospheric transport into the Pacific. The observation-based estimate for Bering Strait transport is 0.8–1.0 Sv, which is much lower than the modeled 1.5 Sv. The reason for this overestimation probably is the coarse resolution. In the model Bering Strait is two grid boxes or 113 km wide, while the true width is only 85 km. Furthermore, it is not possible to resolve the topography with only two grid boxes. This suggests that the model Bering Strait is simply too large. However, this may not be the whole story. Also at higher resolutions NEMO is known to produce too high Bering Strait transports. For instance, an ocean-only run using the ORCA025 configuration performed at KNMI (run KNM01 of Barnier et al. 2007) gives a northward transport of 1.33 Sv. This is less than in the EC-Earth runs discussed here, but still much larger than observed.

The same problem occurs at another narrow strait, namely the Strait of Gibraltar. Although only one grid point wide, it has a width of 90 km in the model, compared to only 15 km in reality. As a result modelled in and outflow (1.78 and 1.74 Sv, respectively) are both more than twice as large as the observation-based estimates of respectively 0.78 and 0.67 Sv (Tsimplis, Bryden 2000). As a result too much saline water is flowing from the Mediterranean Sea into the Atlantic, resulting in a positive salinity anomaly that is visible throughout the whole Atlantic Ocean (see Sect. 3.2, Figs. 4, 6). For this strait the high-resolution KNM01 run gives in- and outflows of about 1 Sv, which is much closer to the observed values, but still too high.

We finally present two estimates for the strength of the GS–North Atlantic Current. The first is for a N–S section from the Florida Keys to Cuba, for which the modelled value is around 19 Sv without any seasonal variation, while a recent estimate based on cable measurements (Hamilton et al. 2005) yields 25 Sv. The second is for a N–S section through the North Atlantic Current at 35°W and between 37°N and 53°N. This averages to 40 Sv with a small annual cycle, substantially lower than the observational-based estimates given in Yaremchuk et al. (2001) of 51 Sv with quite large an annual cycle.

Modelled and observed transport values are summarized in Table 3. The general impression from this table is that EC-Earth produces realistic values, although they are at the lower end of the observed range. However, transports through very narrow straits (Bering and Gibraltar) are overestimated due to the limited resolution.

### 3.7 Atlantic overturning

An important part of the climate system is the meridional overturning circulation in the Atlantic (AMOC) and its associated heat transport. Figure 15a shows the simulated overturning cell in PD. Most of the northern sinking takes place south of 60°N. Observations point to maximum sinking in the Labrador and Irminger Seas as well as north of Iceland. It thus appears that sinking occurs too far to the

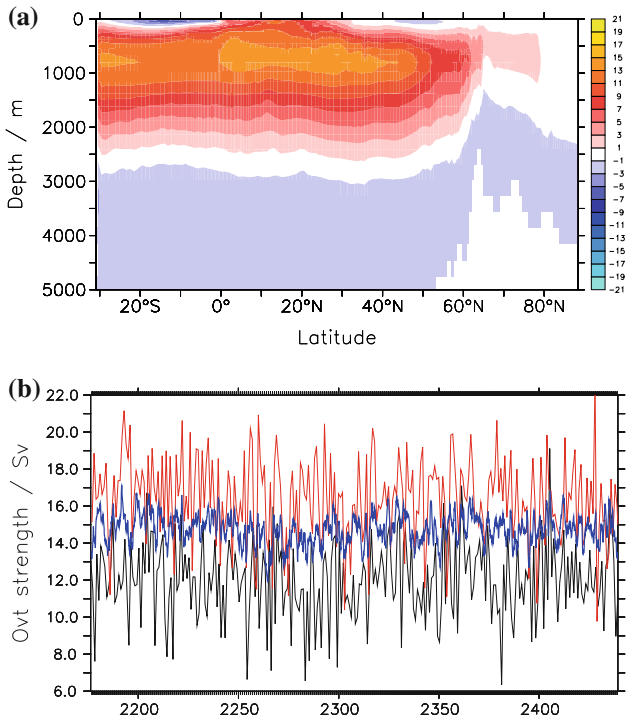


**Fig. 15** **a** Atlantic overturning stream function (in Sv) from PD run. **b** Its strength at 30°N (*black* April, *red* December, *thick blue* annual)

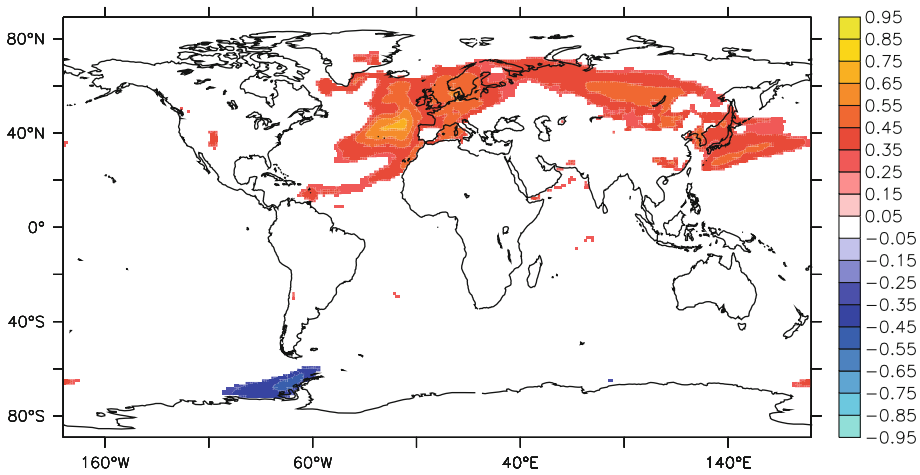


**Fig. 16** Correlation between 10-year running mean AMOC strength and 2 m air temperature in PD. Correlations are only shown where they are significant at the 95% level

south. The maximum of the overturning cell is at a depth of about 800 m, which is too shallow when compared with the observations of Kanzow et al. (2010), who find the maximum at ≈1,100 m. Both results corroborate findings discussed in Sect. 3.2, especially in conjunction with Fig. 4.

We evaluate the strength of the AMOC as the maximum near 30°N of the vertical stream function zonally integrated over the Atlantic (Fig. 15b). The latitude 30°N has been chosen because this is the latitude where the AMOC has it largest strength. The AMOC appears to fluctuate around a mean value of ≈15 Sv with no long-term trend. This is significantly lower than the estimate of 18.7 Sv of Kanzow et al. (2010), based on four years of observations at 26.5°N, but in agreement with both the northward transport of thermocline water and the rate of deep water formation in the North Atlantic. Based on the WOCE dataset both are estimated to be between 14 and 16 Sv (Ganachaud, Wunsch 2000). Kanzow et al. (2010) find quite a large seasonal cycle in the strength of the AMOC with a peak-to-peak amplitude of almost 7 Sv between spring and autumn. The modelled variation is comparable with lowest values in April of ≈11 Sv and maxima in December of ≈17 Sv. Note that there is a large interannual variation in the monthly values (see Fig. 15b).

Ocean-only versions of the NEMO model produce AMOC strengths of a comparable size. Smith et al. (2010a, b), using the ORCA1 configuration, report AMOC strengths of 13–14 Sv and 12 Sv, respectively. While the latter value is for 1 year only, the same value is reported by Biastoch et al. (2008) for a longer period, also for the ORCA1 configuration. For the ORCA025 configuration Barnier et al. (2007) find between 12 and 17 Sv, depending on the applied forcing. So EC-Earth produces a stronger AMOC than comparable ocean-only runs. In the light of the forcing dependency found by Barnier et al. (2007), this might indicate that the forcing provided by the coupled model is realistic.

From Table 3 we see that both the strength of the NAC and that of the AMOC is stronger in PI than in PD, while the transport through Florida Strait is the same. We can only speculate about the reasons, but it might be that the larger cooling in PI north-east of Iceland (see Fig. 3e) creates more sinking, leading to a stronger MOC, while the wind-driven flow through Florida Strait is not affected.

SST in the North Atlantic is known to vary on long (multi-decadal) time scales (Atlantic Multidecadal Oscillation, AMO). Model results show that these variations are connected to changes in the strength of the Atlantic Meridional Overturning Circulation (AMOC) (Vellinga and Wu 2004; Cheng et al. 2004; Delworth and Greatbatch 2000; Jungclaus et al. 2005, and others). We investigate whether similar variability is present in EC-Earth. From Fig. 15b we see that the overturning strength exhibits decadal variations with an amplitude of about 2 Sv, and Fig. 16 shows that these variations are related to temperature variations in large parts of northern Eurasia. A stronger AMOC carries more heat to high latitudes where it is released, heating the atmosphere. In the Southern Hemisphere the signal is weak and predominantly negative with some small peaks near the coast of Antarctica. This is the characteristic signature of the AMO found in the model studies cited above.

The AMOC also influences, and is influenced by, decadal variations of sea ice conditions in parts of the Arctic. Figure 17 shows that the correlation between 10-year running mean values of the AMOC and sea ice thickness at lag 0 is negative. This pattern of correlations is characteristic for a range of lags, but the correlations peak at different lags in different parts of the region. In the Barents and Kara Seas the peak (highest negative correlation) occurs when AMOC leads by about 2 years. The larger than normal northward ocean heat transport during anomalously strong AMOC events leads to less sea ice. Along the East Greenland Current and in the Labrador Sea the

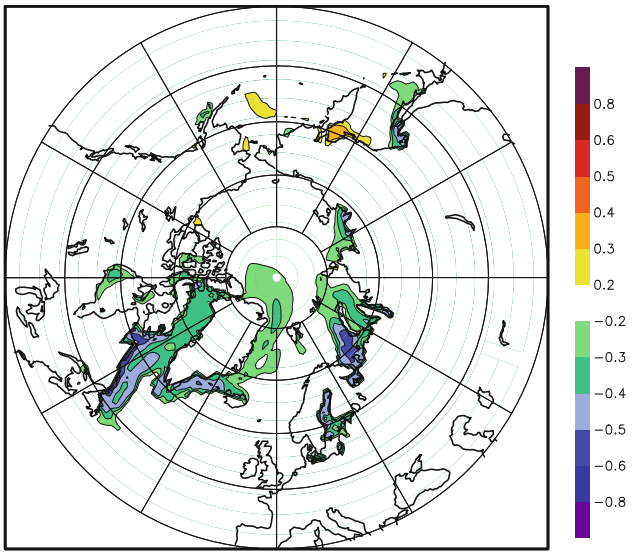


**Fig. 17** Correlation between 10-year running mean AMOC and sea ice thickness in PD run

correlations peak when AMOC lags by a few years, indicating a suppression of the AMOC following years of large ice amounts in those regions.

A mechanism behind this relationship is suggested by Fig. 18. It shows the difference in averaged mixed layer depth between years following respectively high and low ice export through Fram Strait. The correlations between 10-year running mean values of Fram Strait ice export and MLD in the Labrador Sea peak at lag 2 with values reaching up to −0.6. Another 5 years later, at lag 7, 10-year running mean values of the AMOC are correlated with the Fram Strait ice export at −0.5. Enhanced ice export through Fram Strait leads to a freshening of the surface layers, which inhibits deep convection, and reduced deep convection reduces the strength of the AMOC. Model simulations by Haak et al. (2003) and Häkkinen (1999) strongly suggest that the so-called Great Salinity Anomaly (GSA) in the early 1970s (Dickson et al. 1988) was a result of extremely high Fram Strait ice exports during preceding years. From a number of observations taken in the subpolar gyre during the GSA, Dickson et al. (1988) concluded that it is very likely that the GSA had a substantial impact on the deep water formation in the North Atlantic.

While 10-year running mean values of ice export and AMOC and MLD are highly correlated, correlations of annual mean Fram Strait ice export with MLD and AMOC are much weaker, although still significant (not shown). This indicates that only the low-frequency variability of Fram Strait ice export has an effect on AMOC strength. It needs several years of anomalous export to influence the AMOC.

A more detailed investigation of the AMOC and its variability can be found in the paper by Wouters et al. (Clim. Dyn., submitted).

### 3.8 Meridional heat transport

For the climate system the ocean heat transport is very important. The average meridional heat transport (MHT) for the different ocean basins as a function of latitude for the last 100 years of PD is shown in Fig. 19. The MHT for each basin is compared with three observation-based estimates in Table 4. Ganachaud and Wunsch (2000) (GW in the following) obtained consistent estimates of volume and heat transports at a number of WOCE-sections using hydrographic inverse box models. Trenberth and Caron (2001) (TC in the following) apply an alternative method. They calculate the ocean heat convergence as the residual

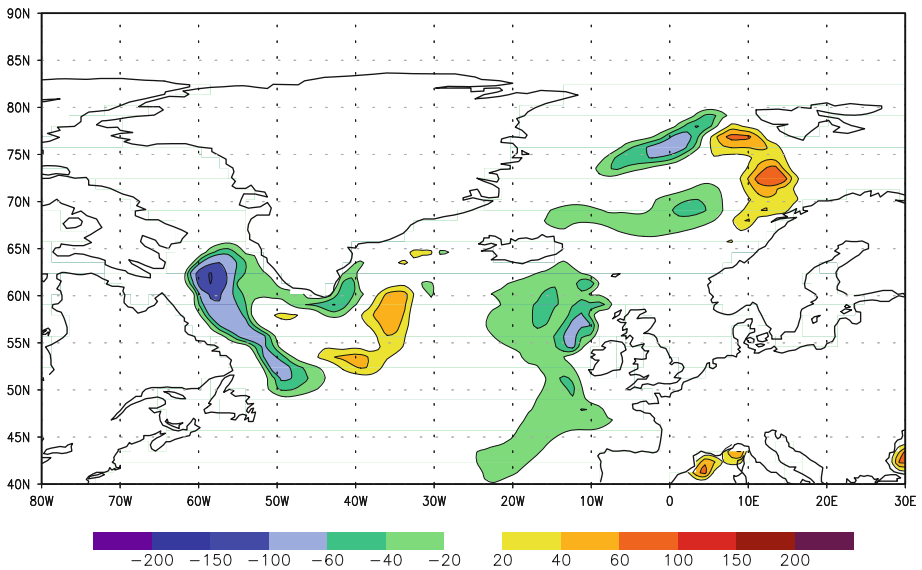


**Fig. 18** Composite difference map of the 10-year averaged mixed layer depth field (in m) for high Fram Strait sea ice exports (>1 $\sigma$) minus low ice exports (<−1 $\sigma$) in PD. The ice export is leading by 2 years

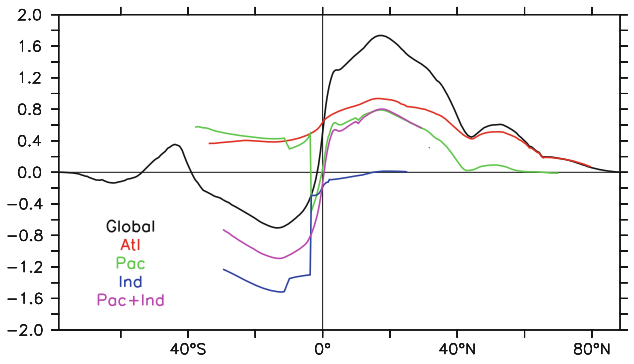


**Fig. 19** Meridional ocean heat transport (in PW) as a function of latitude (run PD) for different ocean basins as indicated in the *plot*. The Pacific and Indian basins are connected via the Indonesian Throughflow at 5°S. The accompanied heat transport is reflected by the large negative spike in the Pacific transport and the associated jump in the Indian transport at that latitude

**Table 4** Estimated meridional heat transports (in PW, positive northward) for run PD and from observation-based estimates

| Basin | PD | | GW | | TC-N | | TC-E | |
|---|---|---|---|---|---|---|---|---|
| NAtl | 1.0 | 20°N | 1.3 | 25°N | 1.2 | 20°N | 0.9 | 20°N |
| SAtl | 0.4 | | 0.3-1 | | 0.7 | | 0.4 | |
| NPac | 0.9 | 10°N | 0.5 | 20°N | 0.9 | 10°N | 0.7 | 10°N |
| SPac | 0.4 | | 0.2-0.6 | | | | | |
| SInd | −1.6 | 10°S | −1.6 | | | | | |
| SInd+SPac | −1.2 | 10°S | −1.4 to −1.0 | | −1.9 | 10°S | −1.7 | 10°S |

*GW* Ganachaud and Wunsch 2000, *TC-N and TC-E* Trenberth and Caron (2001), based on NCEP/NCAR and ERA-40 reanalysis, respectively. Note that the TC estimates are only meaningful for a semi-enclosed basin. Therefore, only a combined value for the Pacific and Indian Oceans is given. If a clear maximum exists we give the heat transport at the maximum, together with the latitude. Otherwise, we give an approximate value valid for a range of latitudes

from combining the atmospheric heat convergence obtained from reanalyses and the top-of-atmosphere radiative balance from ERBE. The ocean heat convergence is then integrated to get an estimate of the MHT. This integration requires a semi-enclosed basin and therefore works for the Atlantic, but not for the Pacific and Indian Oceans separately as they are connected by the non-negligible Indonesian Throughflow. In the table we therefore give only values for the combination of the two basins. As TC use both the NCEP/NCAR and the ERA-40 reanalysis, they obtain two estimates of the MHT.

As can be seen from Table 4 the meridional heat transports as obtained from the PD run are generally compatible with the observation-based estimates. It should be noted that the latter display a large range between the different estimates. In the North Atlantic simulated values are at the lower end of the range of observation-based estimates, while in the North Pacific they are at the higher end. In the SH simulated values are in good agreement with GW, but substantially lower than TC.

In agreement with GW a northward heat transport is simulated in the South Pacific. A large part of this transport is lost to the Indian Ocean via the Indonesian Throughflow, for which GW give a value of 1.4 PW. This is in good agreement with the simulated value which can be deduced from the height of the spike near 5°S in the green (Pacific) curve of Fig. 19 and the accompanying jump in the blue (Indian) curve. The definition of the Pacific and Indian basins is such that they are connected at 5°S across the Indonesian Archipelago.

EC-Earth simulates a northward heat transport south of 40°S (Fig. 19) as a direct consequence of the positive air-sea heat flux simulated in this region (Fig. 9). It is not supported by TC, while GW do not have sections south of 30°S.

### 3.9 ENSO

EC-Earth exhibits the coupled atmosphere-ocean El Niño-Southern Oscillation (ENSO) phenomenon. This is illustrated in Fig. 20 by the NINO-3.4 index (SST anomaly averaged over 170°W–120°W, 5°S–5°N) calculated from observations (Kaplan et al. 1998) over the recent ca. 150 years and from a 150 year segment from the late part of the PD run.

Although the two records look qualitatively similar, there are important differences. Defining an El Niño event as an average winter anomaly of the NINO-3.4 index above 0.5°C (Trenberth 1997), there is an average time span of 5 years between El Niño events in the model, while it is 3.8 years in the observational record. For La Niña events the time span is 3.9 years in the model and 3.7 years in observations. Thus both El Niño and La Niña events of a certain strength are less frequent in the model than in observations. In other words, the modelled ENSO-episodes are weaker than in observations. The modelled and observed annual cycles of ENSO compare well (not shown). Both have their maximum in January.

To assess the realism of the modelled SST-pattern for ENSO, we compare modelled and observed SST composites (Fig. 21). Obviously the SST imprint of El Niño events is qualitatively similar in observations and in EC-Earth. However, the model signal is too much confined around the equator and it is weaker than in the observations. This is in agreement with our previous results. A similar conclusion holds for the La Niña events (not shown).

The development of ENSO is illustrated in Fig. 22. It shows how temperature anomalies are generated in the warm pool region of the western equatorial Pacific and travel along the thermocline to the east, where they surface and can generate an ENSO (either El Niño or La Niña)

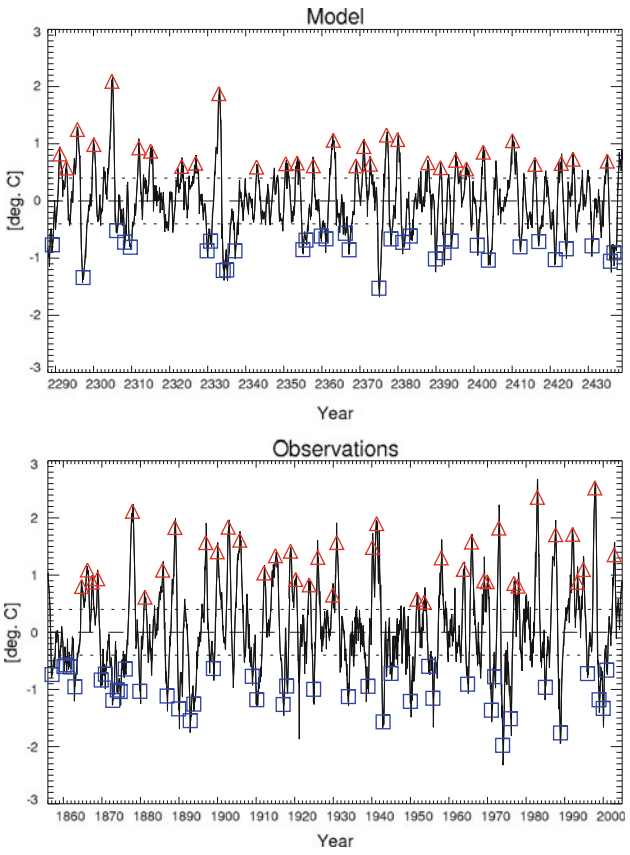


**Fig. 20** NINO-3.4 index (average of SST anomalies over the region 170°E–120°E, 5°S–5°N) calculated from the PD run of EC-Earth (*upper*) and from observations (*lower*)

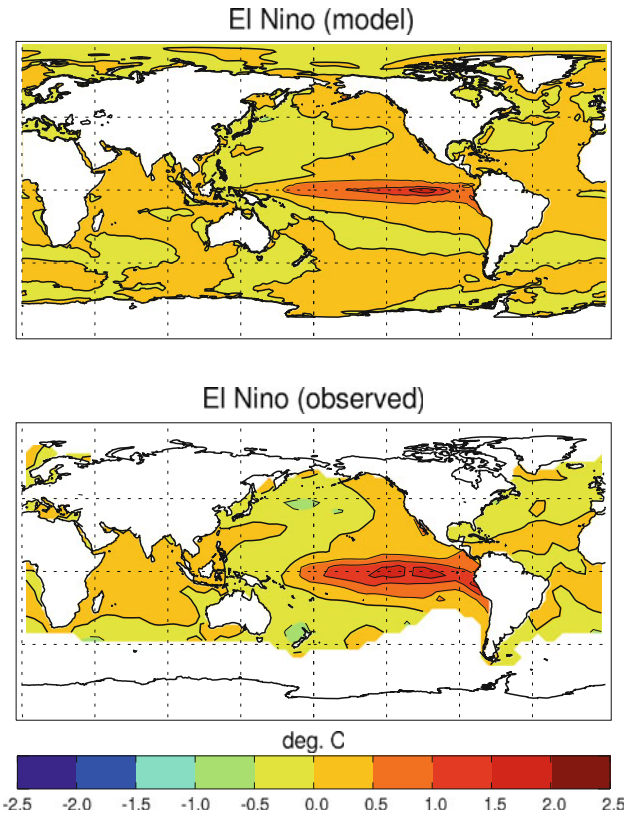


**Fig. 21** SST-composite map of El Niño events in EC-Earth run PD (*upper*) and in observations (*lower*)

event. However, not every anomaly arriving in the eastern Pacific generates an event. Take for example the development during year 2277. A warm anomaly starts in January and reaches the East in April. As it is not spreading westward at the surface, it only raises the NINO3.4 index to 0 (first panel of Fig. 22). The following cold anomaly does spread at the surface (July and October) and drives the NINO3.4 index back to −0.8. The following warm anomaly is much stronger. It reaches the surface in April 2278 and drives the NINO3.4 index to +0.4. About 1 year later the index reaches a maximum of about 1.2, but this large El Niño ends abruptly when the next cold anomaly arrives by the end of 2279.

## 4 The cold event

Besides the two runs (PD and PI) discussed in this paper, several other runs with EC-Earth have been performed. They start from different initial conditions and employ different forcings. In one of them, conducted by Met Éireann, an interesting cold event occurred, which will shortly be presented here. The run was initialized with observed T and S fields (WOA 2001; Conkright et al. 2002) for the ocean and ERA-40 data from the 1st of January, 1979 for the atmosphere and performed with pre-industrial (1850) GHG and aerosol concentrations. Other parameters were as in PI and PD. The simulation was run for 1,125 years and the cold event begins to appear after approximately 450 years. It evolves smoothly, albeit rapidly, suggesting that it is not an artifact caused by an external error during the run. Its occurrence could not be reproduced after a computer upgrade. It has to be regarded as an example of the chaotic nature of the climate system.

The cold anomaly is most evident across an area from the Barents Sea to the Greenland and Iceland Seas as far as Baffin Bay. The sudden cooling is clearly evident in the 10 year running mean time series of the AMO index (SST anomaly over the area 60°W to 5°W and 0°N to 60°N) as shown in Fig. 23a as well as in the AMOC (Fig. 23b). Note that the AMOC strength in this run gradually converges from very high initial values to about 15 Sv, a value comparable to those found for the PD and PI runs. Remember that the initial conditions were taken from observations rather than from a long spin-up run as for PD and PI. The model needs some time to adjust to its apparent intrinsic overturning strength of about 15 Sv. The cold event is superimposed on this slow adjustment.

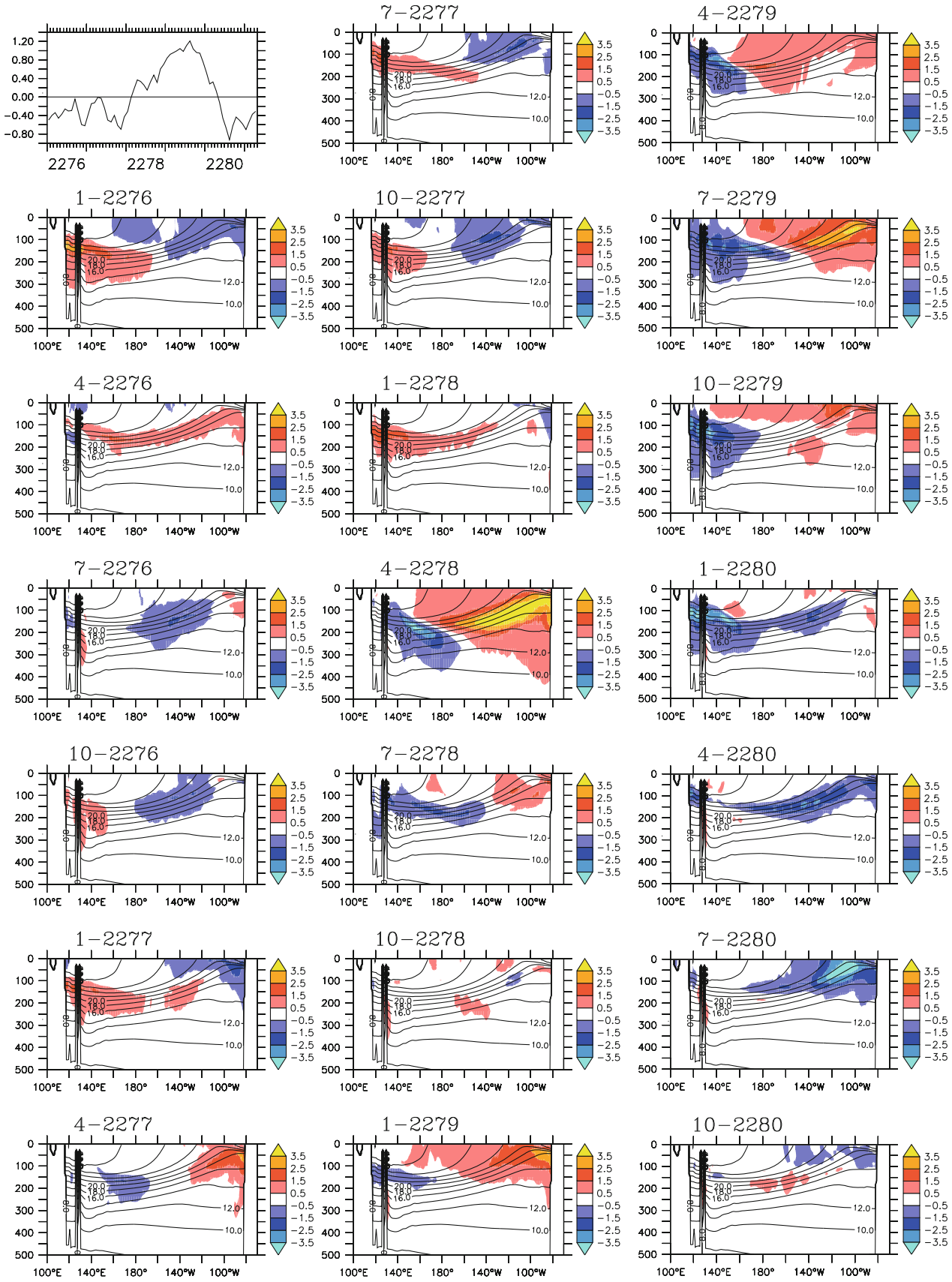
1.20
0.80
0.40
0.00
−0.40
−0.80
2276
2278
2280
7−2277
4−2279
1−2276
10−2277
7−2279
4−2276
1−2278
10−2279
7−2276
4−2278
1−2280
10−2276
7−2278
4−2280
1−2277
10−2278
7−2280
4−2277
1−2279
10−2280
0
100
200
300
400
500
100°E
140°E
180°
140°W
100°W
3.5
2.5
1.5
0.5
−0.5
−1.5
−2.5
−3.5
20.0
18.0
16.0
12.0
10.0
8.0

◀ **Fig. 22** Evolution of ENSO events. The *upper left panel* shows 4 years of the NINO3.4 index (in K). The *other panels* are longitude-depth sections at the equator in the Pacific, showing in steps of 3 months the evolution of temperature anomalies (*color*, in K) as they travel from west to east along the thermocline (*isolines* climatological temperature) across the equatorial Pacific. The *labels* denote month and year

A study of 50 year periods before (years 41–90), during (years 461–510) and after (651–700) the cold event shows that during the event the mean sea level pressure is lower over western Europe, but higher over an area around southern Greenland. This results in a stronger westerly component of the 10m wind over western Europe (not shown), a stronger northerly airflow over an area stretching from Svalbard to Iceland and south Greenland, and more southerly flow to the west of Greenland (Fig. 24).

The enhanced northerly airflow causes temperatures to drop by up to 12 K and sea ice to grow (Fig. 25) south of Greenland. Both effects probably reinforce each other. Due to the enhanced sea ice cover, the anomalous southerly winds west of Greenland (Fig. 24) do not lead to a warming in this region. In all cases, the difference between the cold event period and pre-cold event period are similar to those for the cold event period and post-cold event period.

It should be noted that the temperature patterns shown in the Fig. 25b and in Fig. 16 are similar, while their amplitude is much larger (and of course negative) in the cold-event case. This indicates that a stronger AMOC anomaly

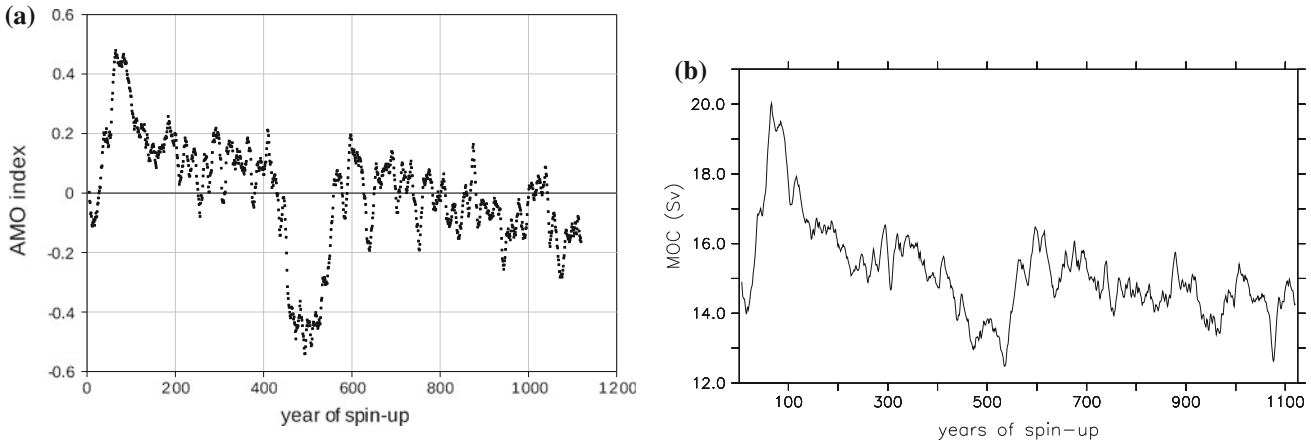


**Fig. 23** Time series of a 10 year running mean of **a** the AMO index (SST anomaly over the area 60°W to 5°W and 0°N to 60°N, in K), and **b** the AMOC strength (in Sv) at 30°N in the Met Éireann run

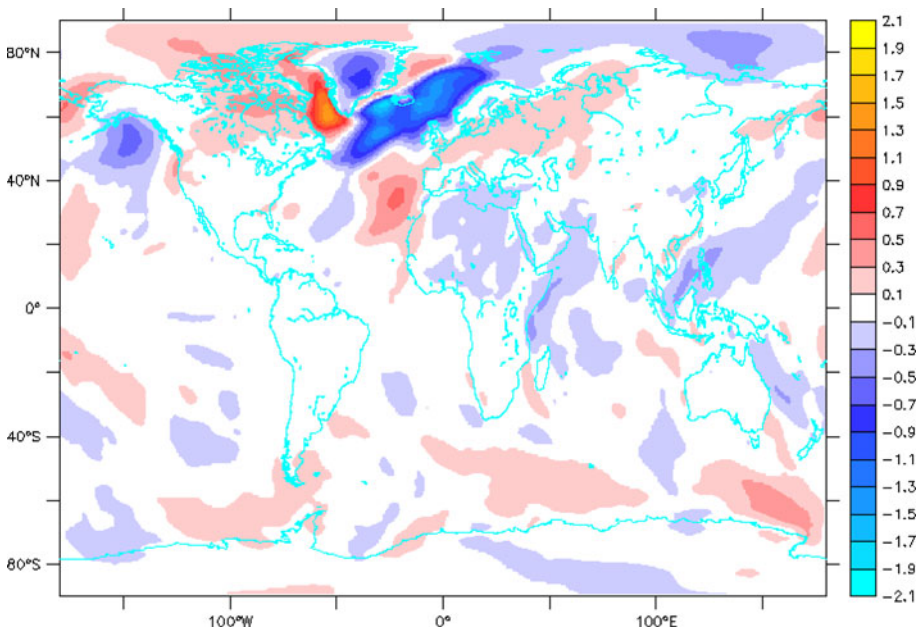


**Fig. 24** Mean difference (in m/s) between the v-component of 10m wind for the cold event period and pre-cold event period. The months of November to March were included in the calculation

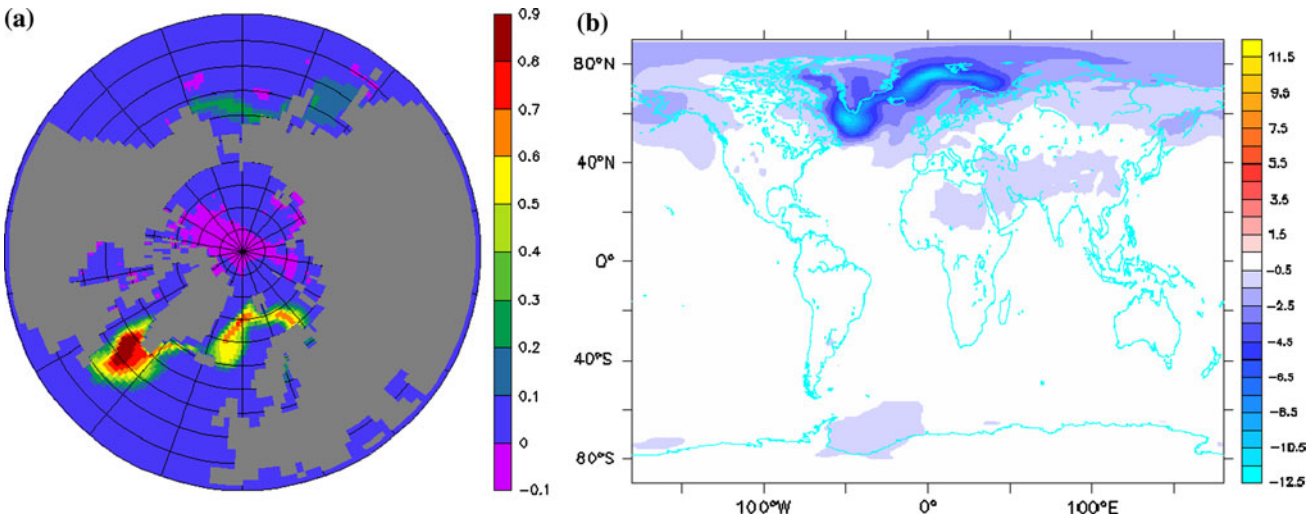


**Fig. 25** Mean difference of **a** the sea ice cover (fraction) and **b** 2m-temperature (in K) between the cold event period and pre-cold event period. The months of November to March were included in the calculation

leads to a stronger response in the atmosphere, but that this response is confined to approximately the same region.

A full analysis of the cold event will be given in a paper by Gleeson et al. (in preparation).

## 5 Summary and conclusion

EC-Earth is an Earth System Model developed by a consortium of several European institutes. Using a numerical weather prediction model (the Integrated Forecast System of ECMWF) as its atmospheric component it tries to bridge the gap between weather prediction and climate modelling and make "seamless prediction" feasible. This paper focuses on the evaluation of the ocean part of EC-Earth, which is formed by the NEMO/LIM ice-ocean model. Both the atmosphere and the ocean component have a horizontal resolution of about 1°.

The mean state (temperature, salinity circulation, sea ice) of the ocean is generally captured well in the coupled model. At the surface the ocean is generally too fresh, and SST biases vary between slightly too cold equatorward of 40° and too warm outside of this region. The warm bias can be traced back to too much warming and too little mixing in the Southern Ocean and too broad and wrongly positioned currents (Kuroshio and GS) in the Northern Hemisphere. Additionally a warm bias is found in the upwelling areas along the eastern margins of the ocean basins, where too little cloud cover leads to excessive solar warming. With the exception of the large positive SST bias in the SO all biases are within the range experienced by climate models of comparable complexity.

In the interior ocean the largest deviations from climatological values occur in the Atlantic, which is too warm and salty at depths between about 800 m at around 40°N and up to 2,000 m in its southern part. The origin of this anomaly is a Mediterranean outflow which, while having realistic T and S values, is more than a factor of two too strong. This is a direct effect of the limited model resolution, due to which the Strait of Gibraltar is 90 km wide as compared to only 15 km in reality. The same resolution problem leads to too high a transport through Bering Strait.

While transports through small straits are over-estimated, the strength of the general circulation as for instance measured by the transport through Drake Passage or the strength of the Atlantic Meridional Overturning Circulation (AMOC) appears to be at the lower end of observational estimates. Despite this the simulated meridional heat transports have realistic values.

While turbulent surface fluxes of heat and momentum are in good agreement with climatologies, the solar flux (shortwave radiation) is generally overestimated. This is mainly due to cloud-related flaws in the atmosphere model, particularly in the mid-latitude eastern boundary regions. In general, this excess of heat input is rather well balanced by an increase of non-solar heat losses.

In the Arctic, sea ice conditions are well simulated in EC-Earth as compared to other global climate models. Around Antarctica the amount of sea ice is underestimated due to the too warm surrounding water masses.

While the Arctic sea ice extent is well simulated, the ice thickness tends to be somewhat overestimated, particularly at the Siberian coast. This is a typical feature of coupled climate models. The Fram Strait sea ice export shows realistic values both regarding the mean and inter-annual variations. High sea ice exports cause reduced convection particularly in the Labrador Sea and are thus potentially affecting the AMOC. On the other hand, decadal AMOC

variations are strongly affecting the air temperature in the North Atlantic area and the surrounding land masses and induce sea ice variations in the Atlantic sector of the Arctic.

ENSO variability in the tropical Pacific, the largest inter-annual climate signal, is well simulated by EC-Earth. Its amplitude is slightly weaker than seen in observations, and its pattern is too much confined to the Equator. These are typical properties of current coupled climate models.

Overall the performance of the ocean part of EC-Earth is comparable to that of other climate models with a similar complexity. Work to improve the model is underway and will lead to the next version of the model (see below). First results indicate that identified weaknesses will be improved upon in that version.

## 6 Outlook

Within the EC-Earth consortium, the development of EC-Earth will be continued. Development of a new version 3 is ongoing. Thereby we take advantage of the improvements made in the components of EC-Earth.

For the atmosphere, an upgrade from IFS cycle 31r1 to cycle 36r4 is planned for the coming EC-Earth version 3. The two most distinct changes from version 2 to 3 are the new shortwave radiation scheme (RRTM-SW) with McICA cloud radiation interaction, and a new cloud microphysics scheme with 5 prognostic species.

The new NEMO 3.3 version is used as the ocean component. A number of physical and technical changes and improvements have been made compared to the NEMO-version used in EC-Earth v2.2 (based on NEMO2). These include for instance a new improved TKE scheme, an improved diurnal cycle, lateral mixing, a new way to handle the atmospheric pressure and a new river input scheme.

Atmospheric forced ocean stand-alone simulations show that the new NEMO-version leads to an improvement in the SST bias in the SO.

Another very important improvement is the use of the new sea ice model LIM3 (Vancoppenolle et al. 2008) instead of LIM2. Major changes in LIM3 are the use of multi-category sea ice classes, the explicit treatment of the salinity cycle and the use of a C-grid elastic-viscous plastic rheology instead of a B-grid plastic-viscous rheology. Simulations with a stand-alone ocean-sea ice model (Vancoppenolle et al. 2008) have shown that the improvements lead to a better annual sea ice cycle with more realistic summer sea ice melt and a reduction of the positive sea ice bias at the Siberian coast.

**Acknowledgments** We thank ECMWF (Reading, UK), IPSL (Paris, France) and CERFACS (Toulouse, France) for providing us with the IFS, NEMO and OASIS codes, respectively. Simona Ştefănescu (ECMWF), Sébastien Masson (IPSL) and Sophie Valcke (CERFACS) provided valuable advice in using them. Computing time to run the model has been provided by ECMWF and ICHEC (Irish Centre for High End Computing). The Kaplan SST V2 data were provided by NOAA/OAR/ESRL PSD (Boulder, Colorado, USA) via their web site (http://www.esrl.noaa.gov/psd). A large part of the plotting was done using Ferret, which is available from NOAA/PMEL at http://www.ferret.noaa.gov. Part of the analysis was done using the CDF-TOOLS package, which was kindly provided by J.M. Molines, Laboratoire des Ecoulements Géophysiques et Industriels, Grenoble, France. TS received funding from the European Community's 7th Framework Programme (FP7/2007-2013) under grant agreement No. GA212643 (THOR: "Thermohaline Overturning at Risk", 2008–2012).

## A Flux coupling in EC-Earth

Global conservative regridding of a flux $F$ requires that

$$F = F^*, \tag{1}$$

where the asterisk indicates the flux after regridding. The fluxes can be written as the sum over all grid cells in the source and target grids, respectively,

$$F = \sum_i f_i A_i, \tag{2}$$

$$F^* = \sum_j f_j^* A_j^*. \tag{3}$$

where $f$ is the grid cell mean flux and $A$ is the grid cell area. Each grid cell can consist of a number of tiles (surface types) with fractional area $\alpha_t$ ($\alpha_t^*$), so that

$$F = \sum_i \sum_t \alpha_{i,t} f_{i,t} A_i, \tag{4}$$

$$F^* = \sum_j \sum_t \alpha_{j,t}^* f_{j,t}^* A_j^*. \tag{5}$$

Since both summations have a finite range, they can be swapped

$$F = \sum_t \sum_i \alpha_{i,t} f_{i,t} A_i, \tag{6}$$

$$F^* = \sum_t \sum_j \alpha_{j,t}^* f_{j,t}^* A_j^*. \tag{7}$$

In the coupling, flux conservation should be guaranteed for each tile type,

$$\sum_i \alpha_{i,t} f_{i,t} A_i = \sum_j \alpha_{j,t}^* f_{j,t}^* A_j^*. \tag{8}$$

The atmosphere model computes the fluxes $f_{i,t}$ for each tile and each grid cell of the atmospheric grid. The tile fractions for land are prescribed and those of the open ocean and sea ice are received from NEMO. The latter are given for the binary ocean mask used by NEMO. The fractions

are adjusted to match the land distribution so that the total of land, ocean and sea ice is everywhere equal to one in IFS.

IFS sends the tile fractions $\alpha_{i,t}$ and the tile fraction weighted fluxes $\alpha_{i,t}\ f_{i,t}$ to NEMO using the first order conservative regridding method of OASIS. This regridding method takes care of the area weights and is locally conservative. This latter property implies that the last equation above is also valid for a single grid cell in the target grid and can be simplified to

$$\sum_i \alpha_{i,t} f_{i,t} A_i w_{i,j} = \alpha^*_{j,t} f^*_{j,t} A^*_j, \tag{9}$$

where $w_{i,j}$ is the overlap of the grid cell $i$ in the source grid and the grid cell $j$ in the target grid.

The coupling now works as follows: IFS computes the fluxes for each grid cell and tile type and sends the fields $\alpha_{i,t}$ and $\alpha_{i,t}\ f_{i,t}$ to NEMO,

$$\alpha_{i,t} \rightarrow \alpha^*_{j,t}, \tag{10}$$

$$\alpha_{i,t} f_{i,t} \rightarrow (\alpha_{j,t} f_{j,t})^* \equiv \alpha^*_{j,t} f^*_{j,t}, \tag{11}$$

and NEMO computes the flux for each grid cell and tile type as

$$f^*_{j,t} = (\alpha_{j,t} f_{j,t})^* / \alpha^*_{j,t}. \tag{12}$$

## References


Antonov JI, Seidov D, Boyer TP, Locarnini RA, Mishonov AV, Garcia HE, Baranova OK, Zweng MM, Johnson DR (2010) World Ocean Atlas 2009, volume 2: Salinity. In: Levitus S (ed) NOAA Atlas NESDIS 69. U.S. Government Printing Office, Washington, DC

Arakawa A, Lamb VR (1977) Computational design of the basic dynamical processes of the UCLA General Circulation Model. Meth Comp Phys 17:173–265

Balsamo G, Viterbo P, Beljaars A, van den Hurk BJJM, Betts A, Scipal K (2009) A revised hydrology for the ECMWF model: Verification from field site to terrestrial water storage and impact in the integrated forecast system. J Hydrometeorol 10:623–643

Barnier B, Brodeau L, Le Sommer J, Molines J-M, Penduff T, Theetten S, Treguier A-M, Madec G, Biastoch A, Böning C, Dengg J, Gulev S, Bourdallé Badie R, Chanut J, Garric G, Alderson S, Coward A, de Cuevas B, New A, Haines K, Smith G, Drijfhout S, Hazeleger W, Severijns C, Myers P (2007) Eddy-permitting ocean circulation hindcasts of past decades. Clivar Exchanges 12:8–10

Bechtold P, Köhler M, Jung T, Leutbecher M, Rodwell M, Vitart F, Balsamo G (2008) Advances in predicting atmospheric variability with the ECMWF model, 2008: From synoptic to decadal time-scales. Q J R Meteorol Soc 134:1337–1351

Belchansky GI, Douglas DC, Platonov NG (2008) Fluctuating Arctic sea ice thickness changes estimated by an in-situ learned and empirically forced neural network model. J Clim 21:716–729. doi:10.1175/2007JCLI1787.1

Biastoch A, Böning C, Getzlaff J, Moline J-M, Madec G (2008) Causes of interannualdecadal variability in the meridional overturning circulation of the Midlatitude North Atlantic Ocean. J Clim 21:6599–6615. doi:10.1175/2008JCLI2404.1

Bouillon S, Morales Maqueda MA, Legat V, Fichefet T (2009) An elastic-viscous-plastic sea ice model formulated on Arakawa B and C grids. Ocean Modell 27:174–184. doi:10.1016/j.ocemod.2009.01.004

Cavalieri D, Parkinson C, Gloersen P, Zwally HJ (1996) Sea ice concentrations from Nimbus-7 SMMR and DMSP SSM/I passive microwave data. National Snow and Ice Data Center. Digital media, Boulder (updated 2008)

Cheng W, Bleck R, Rooth C (2004) Multi-decadal thermohaline variability in an ocean-atmosphere general circulation model. Clim Dyn 22:573–590

Conkright ME, Locarnini RA, Garcia HE, OBrien TD, Boyer TP, Stephens C, Antonov JI (2002) World Ocean Atlas 2001: objective analyses, data statistics, and figures, CD-ROM documentation. National Oceanographic Data Center, Silver Spring

Cunningham SA, Alderson SG, King BA, Brandon MA (2003) Transport and variability of the Antarctic circumpolar current in Drake passage. J Geophys Res 108(C5):8084. doi:10.1029/2001JC001147

Delworth TL, Greatbatch RJ (2000) Multidecadal thermohaline circulation variability driven by atmospheric surface flux forcing. J Clim 13:1481–1495

DeWeaver E, Bitz CM (2006) Atmospheric circulation and Its effect on Arctic Sea Ice in CCSM3 simulations at medium and high resolution. J Clim 19:2415–2436

Dickson R, Meincke J, Malmberg SA, Lee A (1988) The "great salinity anomaly" in the northern North Atlantic, 1968–1982. Progr Oceanogr 20:103–151

Dong S, Sprintall J, Gille ST, Talley L (2008) Southern ocean mixed-layer depth from Argo float profiles. J Geophys Res 113:C06013. doi:10.1029/2006JC004051

Dutra E, Balsamo G, Viterbo P, Miranda PMA, Beljaars A, Schär C, Elder K (2010) An improved snow scheme for the ECMWF land surface model: description and offline validation. J Hydrometeorol 11:899–916. doi:10.1175/2010JHM1249.1

ECMWF (2006) IFS documentation. Available at http://www.ecmwf.int/research/ifsdocs/CY31R1/index.html

Fichefet T, Morales Maqueda MA (1997) Sensitivity of a global sea ice model to the treatment of ice thermodynamics and dynamics. J Geophys Res 102:12,609–12,646. doi:10.1029/97JC00480

Ganachaud A, Wunsch C (2000) Improved estimates of global ocean circulation, heat transport and mixing from hydrographic data. Nature 408:453–457

Gent PR, McWilliams JC (1990) Isopycnal Mixing in Ocean Circulation Models. J Phys Oceanogr 20:150–155

Gibson JK, Kållberg P, Uppala S, Hernandez A, Nomura A, Serrano E (1997) ERA description. ECMWF reanalysis project report 1, ECMWF, Reading, UK, 72 pp

Gnanadesikan A, Hallberg RW (2000) On the relationship of the circumpolar current to southern hemisphere winds in coarse-resolution ocean models. J Phys Oceanogr 30:2013–2034

Goosse H, Selten F, Haarsma R, Opstegh J (2002) A mechanism of decadal variability of the sea-ice volume in the Northern Hemisphere. Clim Dyn 19:61–83

Grist JP, Josey SA (2003) Inverse analysis adjustment of the SOC air-sea flux climatology using ocean heat transport constraints. J. Clim 20:3274–3295

Haak H, Jungclaus J, Mikolajewicz U, Latif M (2003) Formation and propagation of great salinity anomalies. Geophys Res Lett 30(9):26/1–126/4

Häkkinen S (1999) A simulation of thermohaline effects of a great salinity anomaly. J Clim 6:1781–1795

Hamilton P, Larsen JC, Leaman KD, Lee TN, E. Waddell E (2005) Transports through the Straits of Florida. J Phys Oceanogr 35:308–322

Hazeleger W, Severijns C, Semmler T, Ştefănescu S, Yang S, Wang X, Wyser K, Dutra E, Baldasano JM, Bintanja R, Bougeault P, Caballero R, Ekman AML, Christensen JH, van den Hurk B, Jimenez P, Jones C, Kållberg P, Koenigk T, McGrath R, Miranda P, van Noije T, Palmer T, Parodi JA, Schmith T, Selten F, Storelvmo T, Sterl A, Tapamo H, Vancoppenolle M, Viterbo P, Willén U (2010) EC-Earth: a seamless earth-system prediction approach in action. Bull Am Meteorol Soc 91:1357–1363. doi:10.1175/2010BAMS2877.1

Hazeleger W, Wang X, Severijns C, Ştefănescu S, Bintanja R, Sterl A, Wyser K, Semmler T, Yang S, Van den Hurk B, Van Noije T, Van der Linden E, Van den Wiel K (2011) EC-Earth V2: description and validation of a new seamless Earth system prediction model. Clim. Dyn. doi:10.1007/s00382-011-1228-5

Huang CJ, Qiao F, Song Z, Ezer T (2011) Improving simulations of the upper ocean by inclusion of surface waves in the Mellor-Yamada turbulence scheme. J Geophys Res 116:C01007. doi:10.1029/2010JC006320

Jungclaus JH, Haak H, Latif M, Mikolajewicz U (2005) Arctic-North Atlantic interactions and multidecadal variability of the meridional overturning circulation. J Clim 18:4013–4031

Kanzow T, Cunningham SA, Johns WE, Hirschi JJ-M, Marotzke J, Baringer MO, Meinen CS, Chidichimo MP, Atkinson C, Beal LM, Bryden HL, Collins J (2010) Seasonal variability of the Atlantic meridional overturning circulation at 26.5°N. J Clim 23:5678–5698. doi:10.1175/2010JCLI3389.1

Kaplan A, Cane M, Kushnir Y, Clement A, Blumenthal M, Rajagopalan B (1998) Analyses of global sea surface temperature 1856–1991. J Geophys Res 103:18567–18589

Koenigk T, Mikolajewicz U, Haak H, Jungclaus J (2006) Variability of Fram Strait sea ice export: causes, impacts and feedbacks in a coupled climate model. Clim Dyn 26:17–34. doi:10.1007/s00382-005-0060-1

Kwok R, Cunningham G, Pang S (2004) Fram Strait sea ice outflow. J Geophys Res 109:C01009. doi:10.1029/2003JC001785

Lavender K, Davis R, Owens W (2002) Observations of open-ocean deep convection in the Labrador Sea from subsurface floats. J Phys Oceanogr 32(2):511–526

Locarnini RA, Mishonov AV, Antonov JI, Boyer TP, Garcia HE, Baranova OK, Zweng MM, Johnson DR (2010) World Ocean Atlas 2009, volume 1: temperature. In: Levitus S (ed) NOAA Atlas NESDIS 68. U.S. Government Printing Office, Washington, DC

Madec G (2008) NEMO ocean engine. Note du Pole de modélisation. Institut Pierre-Simon Laplace (IPSL), Paris, France, No 27 ISSN No 1288–1619

Morawitz W, Sutton P, Worcester P, Cornuelle B, Lynch J, Pawlowitz R (1996) Three-dimensional observations of a deep convective chimney in the Greenland Sea during winter 1988/89. J Phys Oceanogr 26:2316–2343

Randall DA, Wood RA, Bony S, Colman R, Fichefet T, Fyfe J, Kattsov V, Pitman A, Shukla J, Srinivasan J, Stouffer RJ, Sumi A, Taylor KE (2007) Climate models and their evaluation. In: Solomon S, Qin D, Manning M, Chen Z, Marquis M, Averyt KB, Tignor M, Miller HL (eds) Climate change 2007: the physical science basis. Contribution of working group I to the fourth assessment report of the intergovernmental panel on climate change. Cambridge University Press, Cambridge

Risien CM, Chelton DB (2008) A global climatology of surface wind and wind stress fields from eight years of QuikSCAT scatterometer data. J Phys Oceanogr 38:2379–2413

Rothrock DA, Zhang J, Yu Y (2003) The Arctic ice thickness anomaly of the 1990s: a consistent view from observations and models. J Geophys Res 108(C3):30–83. doi:10.1029/2001JC001208

Simmons A, Uppala S, Dee D, Kobayashi S (2007) ERA-Interim: new ECMWF reanalysis products from 1989 onwards. ECMWF Newsletter 110 (Winter 2006/07, 11 pp)

Smith GC, Bretherton D, Gemmell A, Haines K, Mugford R, Stepanov V, Valdivieso M, Zuo H (2010) Ocean reanalysis studies in reading: reconstructing water mass variability and transports. Mercator Ocean Q Newslett 36:39–49

Smith GC, Haines K, Kanzow T, Cunningham S (2010) Impact of hydrographic data assimilation on the modelled Atlantic meridional overturning circulation. Ocean Sci 6:761–774. doi:10.5194/os-6-761-2010

Sprintall J, Wijffels SE, Molcard R, Jaya I (2009) Direct estimates of the Indonesian Throughflow entering the Indian Ocean: 2004–2006. J Geophys Res 114:C07001. doi:10.1029/2008JC005257

Trenberth KE (1997) The definition of El Niño. Bull Am Meterol Soc 78:2771–2777

Trenberth KE, Caron JM (2001) Estimates of meridional atmosphere and ocean heat transports. J Clim 14:3433–3443

Tsimplis MN, Bryden HL (2000) Estimation of transports through the Strait of Gibraltar. Deep Sea Res A 47:2219–2242. doi:10.1016/S0967-0637(00)00024-8

Valcke S (2006) OASIS3 user guide (prism_2-5). CERFACS technical report TR/CMGC/06/73, PRISM Report No 3, Toulouse, France. 60 pp, http://www.prism.enes.org/Publications/Reports-all_editions/index.php#report02

Vancoppenolle M, Fichefet T, Goosse H, Bouillon S, König Beatty C, Morales Maqueda MA (2008) LIM3, an advanced sea-ice model for climate simulation and operational oceanography. Mercator Ocean Q Newslett 28:16–21

Vellinga M, Wu P (2004) Low-latitude fresh water influence on centennial variability of the thermohaline circulation. J Clim 17:4498–4511

Vinje T (2001) Fram strait ice fluxes and atmospheric circulation: 1950–2000. J Clim 14:3508–3517

Wadhams P, Budeus G, Wilkinson J, Loyning T, Pavlov V (2004) The multi-year development of long-lived convective chimneys in the Greenland Sea. Geophys Res Lett 31:L06306. doi:10.1029/2003GL019017

Woodgate RA, Aagaard K, Weingartner TJ (2006) Interannual changes in the Bering Strait fluxes of volume, heat and freshwater between 1991 and 2004. Geophys Res Lett 33:L15609. doi:10.1029/2006GL026931

Worby AP, Geiger CA, Paget MJ, Van Woert ML, Ackley SF, DeLiberty TL (2008) Thickness distribution of Antarctic sea ice. J Geophys Res 113:C05S92. doi:10.1029/2007JC004254

Yaremchuk MI, Nechaev DA, Thompson KR (2001) Seasonal variation of the North Atlantic Current. J Geophys Res 106(C4):6835–6851